EFFECTS OF MICROCHANNEL MANUFACTURING INACCURACIES ON HEAT SINK PERFORMANCE: NUMERICAL AND EXPERIMENTAL INVESTIGATION

A THESIS SUBMITTED TO
THE GRADUATE SCHOOL OF NATURAL AND APPLIED SCIENCES
OF
MIDDLE EAST TECHNICAL UNIVERSITY

BY

CANBERK ÖZTOPRAK

IN PARTIAL FULFILLMENT OF THE REQUIREMENTS
FOR
THE DEGREE OF MASTER OF SCIENCE
IN
MECHANICAL ENGINEERING

OCTOBER 2018

Approval of the thesis:

EFFECTS OF MICROCHANNEL MANUFACTURING INACCURACIES ON HEAT SINK PERFORMANCE: NUMERICAL AND EXPERIMENTAL INVESTIGATION

submitted by **CANBERK ÖZTOPRAK** in partial fulfillment of the requirements for the degree of **Master of Science in Mechanical Engineering Department, Middle East Technical University** by,

Prof. Dr. Halil Kalıpçılar _____
Dean, Graduate School of **Natural and Applied Sciences**

Prof. Dr. M. A. Sahir Arıkan _____
Head of Department, **Mechanical Engineering**

Prof. Dr. İlker Tarı _____
Supervisor, **Mechanical Engineering Dept., METU**

Examining Committee Members:

Prof. Dr. Derek K. Baker
Mechanical Engineering Department, METU _____

Prof. Dr. İlker Tarı
Mechanical Engineering Department, METU _____

Assoc. Prof. Dr. M. Metin Yavuz
Mechanical Engineering Department, METU _____

Asst. Prof. Dr. Özgür Bayer
Mechanical Engineering Department, METU _____

Asst. Prof. Dr. Mehdı Mehrtash
Energy Systems Engineering Department, Atılım University _____

Date: _____

I hereby declare that all information in this document has been obtained and presented in accordance with academic rules and ethical conduct. I also declare that, as required by these rules and conduct, I have fully cited and referenced all material and results that are not original to this work.

Name, Last Name: CANBERK ÖZTOPRAK

Signature :

ABSTRACT

EFFECTS OF MICROCHANNEL MANUFACTURING INACCURACIES ON HEAT SINK PERFORMANCE: NUMERICAL AND EXPERIMENTAL INVESTIGATION

Öztoprak, Canberk
M.S., Department of Mechanical Engineering
Supervisor : Prof. Dr. İlker Tarı

October 2018, 86 pages

Alternative thermal designs of a microwave module constituting six monolithic microwave integrated circuit (MMIC) power amplifiers (PA) chips with total heat dissipation of 195 W is created by applying a single-phase liquid cooling solution with microchannel heat sinks. Four cold plate alternatives are designed with different material selections of copper and aluminum at increasing fin densities of 25 fins per inch and 85 fins per inch. Heat sink performance of the alternative cold plates with microchannels is investigated numerically and experimentally. A post-experiment numerical investigation in order to understand the sources of mismatch between numerical simulations and experimental studies. Detailed investigation on microchannel heat sinks is resulted with detection of manufacturing inaccuracies due to manufacturing limitations. These manufacturing inaccuracies are classified as variations in channel width, channel height and angle of channel inclination. In the post-experimental numerical investigation, these inaccuracies are analyzed for their individual effects on heat sink performance. For the best representation of manufacturing inaccuracies detected in microchannel heat sinks, combinations of the manufacturing inaccuracies are modeled for numerical simulations. The results of the post-experimental numerical simulations resulted in a good match with experimental studies, especially for pressure gradient values. The study provides microchannel heat sink performance variations to be expected with different material selections, different fin densities,

and manufacturing inaccuracies. The study concludes with the design considerations are to be taken into account for a successful thermal design with microchannel heat sinks. To the best of authors knowledge, this study is the first publishing specifically focusing on the effect of manufacturing inaccuracies on heat sink performance.

Keywords: Electronics cooling, One phase flow, microchannels, microfluidic flow, High heat fluxes cooling, CFD, thermal management of GaN based power amplifiers, manufacturing effects on microchannel flow

ÖZ

MİKROKANAL ÜRETİM HATALARININ SOĞUTUCU PERFORMANSINA ETKİSİNİN SAYISAL VE DENEYSEL İNCELEMESİ

Öztoprak, Canberk
Yüksek Lisans, Makina Mühendisliği Bölümü
Tez Yöneticisi : Prof. Dr. İlker Tarı

Ekim 2018 , 86 sayfa

Altı adet monolitik mikrodalga entegre devresi (MMIC) güç yükselteci (PA) çipi ile toplamda 195 W ısı atımına sahip bir mikrodalga modülünün alternatif termal tasarımları gerçekleştirilmiştir. Alüminyum ve bakır malzemeleri kullanılarak farklı fin yoğunluğuna sahip dört alternatif soğuk plaka tasarlanmıştır. Mikrokanala içeren alternatif soğuk plakaların soğutucu performansları nümerik ve deneysel olarak incelenmiştir. Nümerik analizler ve deney sonuçları arasındaki farklılıkların kaynağı araştırılmış ve deney sonrası güncellenen nümerik model ile incelenmiştir. Mikrokanallı soğutucular detaylı incelenmesi sonucunda kanallarda üretim hataları tespit edilmiştir. Bu üretim hataları kanal kanal genişliği, kanal yüksekliği ve kanal eğikliği olarak sınıflandırılmıştır. Bu üretim hataları deney sonrası nümerik simülasyon modeli kullanılarak ayrı ayrı incelenmiştir. Mikrokanallı soğutucularda tespit edilen hataların en gerçekçi şekilde modellenmesi için üretim hataları kombine şekilde modellenerek nümerik olarak incelenmiştir. Deney sonrası nümerik simülasyon sonuçları deney sonuçları başta basınç düşüm değerleri olmak üzere uyumlu çıkmıştır. Bu çalışma farklı malzemelerden üretilen, farklı fin yoğunluklarına sahip ve üretim hataları gözlenen mikrokannallı soğutucularda beklenmesi gereken soğutucu performans değişimlerini sunmaktadır. Bu çalışmada mikrokanallı soğutucular içeren başarılı bir ısıl tasarım için dikkate alınması gereken tasarım hususları sunulmaktadır. Yazarın bilgi sınırları dahilinde olmak üzere, bu çalışma üretim hatalarının mikrokanallı soğutucu perfor-

mansına etkisini inceleyen ilk yayındır.

Anahtar Kelimeler: Elektronik soğutma, tek fazlı akış, mikrokanal, mikroakışkan, yüksek ısı akılı soğutma, CFD, GaN tabanlı güç yükleteçlerin termal yönetimi, mikrokanalda üretim hatalarının ısı-akışkan üzerinde etkileri

To my family.

ACKNOWLEDGMENTS

I would like to express my deep gratitude and appreciation to my supervisor Prof. Dr. İlker Tarı for his guidance, continuous support and encouragement that made this study possible.

I am also thankful to my employer, ASELSAN Inc., providing me with the state-of-the-art equipments for experimental tests of this study and for allowing my absence during my M.Sc. studies by enforcing a contract strictly stating 6 months of non-resignation period.

Further thanks to Mustafa İncebacak, Çağrı Balıkçı, Erkan Kuday, Taylan Eker, Arda Özgen, Ali İlker Işık, Keziban Göksu, Zeynep Eymür, Şebnem Saygıner, Barışcan Tok, Aykut Barış İnci, Tolga Ayyılmaz, Murat Parlak and my other collegues for their support.

I would like to thank to my family; especially my mother Nuray Öztoprak for her unconditional love, caring and patience; my brother Caner Öztoprak for his efforts to keep my spirit up and my father, Mehmet Öztoprak, for his teachings and inspiration. Finally, I want to express my utmost gratitude to my cousins Alper Karasar, Aslı Sağlam, Burak Sağlam and all my friends for the color they bring to my life.

TABLE OF CONTENTS

ABSTRACT v

ÖZ vii

ACKNOWLEDGMENTS x

TABLE OF CONTENTS xi

LIST OF TABLES xv

LIST OF FIGURES xvii

LIST OF ABBREVIATIONS xx

CHAPTERS

1 INTRODUCTION 1

1.1 The Motivation of the Thesis 1

1.2 Literature Review 3

1.2.1 Single Phase Liquid Cooling with Microchannel Heat Sink 3

1.2.2 Manufacturing Methods of liquid Cold Plate with Microchannels 5

1.3 Overview of the Thesis 8

2 THERMAL DESIGN AND NUMERICAL ANALYSIS 11

2.1 Definition of the Thermal Problem and Conceptual Design of Microwave Modules with Microchannels 11

2.1.1 Thermal Characteristics of Radio Frequency Power Amplifiers 14

2.1.2 Diamond Resistors 19

2.1.3 Conceptual Mechanical and Thermal Design of Microwave Module with Microchannels 21

2.1.3.1 PA Chip Locations (Pattern of Microwave Electronics Design) 22

2.1.3.2 Conceptual Design of Microwave Module with Microchannels 23

2.2 Mechanical Design of Microwave Modules with Microchannels 26

2.2.1 CAD Design of Microwave Modules with Microchannels 26

2.2.1.1 CAD Design of Aluminum Modules . 27

2.2.1.2 CAD Design of Copper Modules . . . 30

2.2.2 Overview of Alternative Designs 33

2.3 Numerical Simulations of Design Alternatives 33

2.3.1 Investigation on Simulation Run Speed 34

2.3.2 CFD Model of Numerical Simulations 35

2.3.3 Investigation of Mesh Independence and Flow Regime 39

2.3.4 Results and Discussion of Numerical Simulations . 43

3 EXPERIMENTAL PROCEDURES AND RESULTS 49

3.1 Experimental Setup 49

3.1.1 Manufacturing Microwave Modules with Microchannels 49

3.1.2 Custom Liquid Control Unit and Manufacturing Pressure Transmitter Adapter 52

3.1.3 Equipment and Devices Used in Experiments . . . 54

3.2 Experimental Procedure 55

3.3 Experimental Results 59

3.3.1 Expected Measurement Uncertainty 60

3.3.2 Repeatability Analysis 61

3.4 Discussion of Experimental Results 62

3.4.1 Manufacturing Inaccuracies in Microchannels . . . 65

4 POST-EXPERIMENT INVESTIGATION OF MANUFACTURING ERRORS OF MICROCHANNELS ON HEAT SINK PERFORMANCE 69

4.1 Effect of Channel Width on Performance 69

4.2 Effect of Channel Height on Performance 70

4.3 Effect of Channel Inclination on Performance 71

4.4 Investigation on Combination of Manufacturing Inaccuracies 71

4.5 Discussion of Post-Experiment Investigation of Manufacturing Inaccuracies of Microchannels 72

5 CONCLUSIONS 75

REFERENCES 77

APPENDICES

A TECHNICAL SPECIFICATIONS OF THE COMPONENTS AND EQUIPMENT USED IN EXPERIMENTAL SETUP 81

A.1 Technical Specifications of OMEGA J-Type Thermocouple . 81

A.2 Technical Specifications of Agilent 34970A Data Logger . . 82

A.3 Technical Specifications of WIKA Type A-10 Pressure Transmitter 83

A.4 Technical Specifications of EMC Technology CR0402D CVD Diamond Resistor Chip 20 Watts 84

A.5 Technical Specifications of EMC Technology CT0505D CVD Diamond Resistor Chip 50 Watts 85

A.6 Technical Specifications of Siemens MASSFLO 6000 Coriolis Flowmeter 86

LIST OF TABLES

TABLES

Table 2.1 Predetermined design parameters 24

Table 2.2 Design alternatives and flexible design parameters 25

Table 2.3 Specification of alternative designs 33

Table 2.4 Results of simulation run speed investigation 35

Table 2.5 Results of mesh independence investigation 39

Table 2.6 Reynolds numbers of alternative modules at different sections of flow passage 42

Table 2.7 Results obtained from different flow regime equations 43

Table 2.8 Numerical Simulation Results 47

Table 3.1 Numerical Simulation Results 55

Table 3.2 Experimental Results 60

Table 3.3 Expected uncertainties of the experimental measurements 61

Table 3.4 Experimental runs for repeatability analysis 61

Table 3.5 Avarage percentage repeatability accuracy of experimental measurements 62

Table 3.6 Comparison of experimental results and numerical simulation results 64

Table 4.1 Simulation cases of channel width investigation 70

Table 4.2 Numerical simulation results of channel width investigation 70

Table 4.3 Numerical simulation results of channel height investigation 71

Table 4.4 Numerical simulation results of channel height investigation 71

Table 4.5 Numerical simulation results of combination of manufacturing inaccuracies compared to experimental results 72

Table 4.6 Results of pre-experiment and post-experiment numerical simulations compared to experimental results for module 4 73

LIST OF FIGURES

FIGURES

Figure 1.1 MDT process schematic [6] 4

Figure 1.2 MDT process schematic [6] 5

Figure 1.3 MDT process schematic 8

Figure 2.1 Microwave module layout 12

Figure 2.2 Aluminum module with microchannels prepared for experiments (a) Isometric view (b) Front view in which the microchannel heat sink is visible 13

Figure 2.3 Basic overview of the overall thermal management structure of the unit 13

Figure 2.4 TGF2023-2-10 Mean Lifetime and Thermal Resistances with respect to Heat Dissipation and Base Plate Temperature under Continuous Work (CW) 15

Figure 2.5 Mean lifetime vs channel temperature 16

Figure 2.6 An infrared camera image of the transistor region of a GaN PA chip 17

Figure 2.7 Typical thermal stack-up of a PA chip and microwave module . . . 18

Figure 2.8 Stack-up of the PA chip and microwave module with liquid cooling 18

Figure 2.9 Rated power of CVD diamond chip resistor vs temperature 19

Figure 2.10 Overview of CVD Diamond Chip Resistor 20 Watts 20

Figure 2.11 Overview of CVD Diamond Chip Resistor 50 Watts 21

Figure 2.12 PA placement on microwave module with "seperate triangles layout " 23

Figure 2.13 Example fin structures of MicroCool® Micro Deformation Technology (MDT) 27

Figure 2.14 Aluminum module with two parts 29

Figure 2.15 Aluminum microwave module with 25 FPI fin density after two parts united (a) Isometric view (b) Front view (c) Top view 29

Figure 2.16 Microchannel fin dimensions of aluminum modules with different fin densities (a) 25 FPI fin density (b) 85 FPI fin density 30

Figure 2.17 Copper module with two parts 31

Figure 2.18 Copper microwave module with 25 FPI fin density after two parts united (a) Isometric view (b) Front view 31

Figure 2.19 Copper microwave module with 25 FPI fin density after two parts united (a) Isometric view (b) Front view 32

Figure 2.20 Microchannel fin dimensions of copper modules with different fin densities (a) 25 FPI fin density (b) 85 FPI fin density 32

Figure 2.21 Simple simulation model 34

Figure 2.22 The simulation model for alternative module analyses 36

Figure 2.23 Details of selected mesh network at module mid section (a) Overall module view (b) Zoomed view of three microchannels (c) Zoomed view of one microchannel 40

Figure 2.24 Sections of liquid flow in modules 41

Figure 2.25 The simulation model for alternative module analyses 43

Figure 2.26 Temperature distributions of the module top surfaces (a) Module 1 (b) Module 2 (c) Module 3 (d) Module 4 44

Figure 2.27 Velocity distribution at mid x-plane of liquid passage of the modules
(a) Module 1 (b) Module 2 (c) Module 3 (d) Module 4 45

Figure 2.28 Pressure distribution at mid z-plane of liquid passage of module 4 . 45

Figure 2.29 Velocity distribution at mid z-plane of liquid passage of the modules
(a) Module 1 (b) Module 2 (c) Module 3 (d) Module 4 46

Figure 3.1 Manufactured microwave modules layout 50

Figure 3.2 The module with diamond resistors and cabling 50

Figure 3.3 The thermocouple measurement locations on modules 51

Figure 3.4 The custom liquid control unit 53

Figure 3.5 User Interface of the custom liquid control unit 53

Figure 3.6 The pressure transmitter adaptors 54

Figure 3.7 The assembly of the module and pressure transmitters 56

Figure 3.8 Experimental setup with power supplies before insulation application 56

Figure 3.9 Insulation of module and pressure transmitter adaptors 57

Figure 3.10 Photos of interface board (left) and data acquisition device (right) . 57

Figure 3.11 Real time experimental measurement through data logger software 57

Figure 3.12 Liquid control unit interface (left) and flow meter (right) 58

Figure 3.13 Power supply settings of the diamond resistors with 5 W heat dissipation (left) and 30 W heat dissipation (right) 58

Figure 3.14 Thermal camera image (left) and thermal camera setup (right) . . . 59

Figure 3.15 Module pieces after water jet cutting (a) Module 1 (b) Module 2 . . 65

Figure 3.16 Microscope images of microchannel heat sink of module 1 66

Figure 3.17 Microscope images of microchannel heat sink of module 2 66

Figure 3.18 Microscope images of microchannel heat sink of module 3 67

Figure 3.19 Microscope images of microchannel heat sink of module 4 68

Figure 3.20 Photos of microchannel heat sink of module 4 prior to water jet cutting 68

Figure 3.21 Photo of microchannel heat sinks of modules (left to right in numerical order) 68

LIST OF ABBREVIATIONS

1-D	One Dimensional
2-D	Two Dimensional
3-D	Three Dimensional
CFD	Computational Fluid Dynamics
RF	Radio Frequency
PA	Power Amplifier Chip
RF PA	Radio Frequency Power Amplifier Chip
GaN	Gallium Nitride
GaAs	Gallium Arsenide
SiC	Silicon Carbide
FPI	Fins per Inch (Fin Density)
CAD	Computational Aided Design
GPU	Graphic Processing Unit
CPU	Central Processing Unit

CHAPTER 1

INTRODUCTION

The focus of this thesis study is the investigation of single-phase liquid cooling with microchannel heat sink on electronic warfare subsystem consisted of electronic components with extreme heat fluxes. In this Chapter, the motivation of the study, literature review and overview of the thesis are presented.

1.1 The Motivation of the Thesis

There is a huge increase in demand for better performing electronic components. While their performance increases, their size shrinking due to mobility needs of our century. This inclination results in more challenging thermal management problems for mechanical engineers. The well-known Moore's law described this trend in 1965 by stating that the number of components per integrated circuit is doubled in every year [1]. Moore G. later revised his law by slowing doubling rate to two years [2]. Today the transistors are reduced to nanometer level and there are chips available in the market with more than a billion transistors. The technology is at the edge of physical boundaries due to limitations in material science such as quantum tunneling effects. Even though the transistor dimension is expected to be saturated in the next decade, the performance demand will continue to increase meaning higher heat dissipations per area. The challenge of thermal management of electronic components is not to diminish in foreseeable future.

All electronic components require a thermal management design according to their specifications. There are a lot of alternative electronic cooling techniques from pas-

sive natural convection cooling seen in mobile phones to active forced convection liquid cooling seen in data servers. Electronic warfare applications present some of the most extreme heat fluxes observed in today's industry. The author believes that the efforts towards achieving optimal thermal management solutions for such systems will be beneficial in future consumer market electronics.

In military radar (radio detection and ranging) systems, the power rating of electronic components determines the critical functional performance parameters such as operation range, tracking accuracy and the number of simultaneous mission objects. In electronic warfare systems with electronic attack (EA) capabilities, the electronic and thermal design is even more challenging since to achieve the objective of radar jamming, higher power rated components with wider frequency range are required. In addition, the electronic warfare systems require continuous work (CW) of electronics rather than duty cycle (DC) working of electronics in radars. The power amplifiers (PA) are the core electronic component in these systems and they determine critical performance metrics such as frequency range, jamming capacity, and operating range. Due to their high-performance requirements, PA chips continuously dissipate extremes heat fluxes in the very limited area. Their mean lifetime is directly related to their working temperature. It should be noted that most of these systems also have an additional operation mode called "war mode" in which the systems functions at maximum capacity regardless of lifetime degradation of components. Therefore, the thermal management of EW systems is a challenge and there is always room for improvement. The challenges faced by thermal design engineers are the system characteristics of high packaging density, low mass/volume, long service life, high maximum operating temperature and most importantly extreme heat fluxes of electronic components. In a sense, thermal design is the limiting factor for determining the performance metrics of the systems. Due to their strategical importance and high market values, manufacturing and material costs are not of importance comparing to system parameters of functional performance, maximum working temperature, size, and weight.

In this study, a thermal management design with microchannel single-phase liquid cooling is investigated for a power amplifier module of an electronic warfare system. The motivation of this study is to achieve the best cooling performance for PA chips

using manufacturing methods available in the market while considering the size and weight constraints. The investigation of manufacturing inaccuracies in microchannels and their effect on heat sink performance is another motivation of this study considering the importance of accurate temperature determination for PA chips.

1.2 Literature Review

1.2.1 Single Phase Liquid Cooling with Microchannel Heat Sink

The increasing demand for the high heat flux and compact devices resulted in liquid channels with smaller dimensions. The researches on microscale heat transfer helped the definition of the microchannels. There are several classifications can be found in the literature regarding microchannels. In general, heat sinks with channel dimensions below 1 mm are called microchannels by cold plate manufacturers. Mehendale et al. [3] defined that the channels with a dimension of 1 µm to 100 µm are microchannels whereas mesochannels are within range of 100 µm to 1 mm, compact passages are within range of 1 mm to 6 mm and conventional passages are with dimensions above 6 mm. The classification proposed by Kandlikar [4, 5] focusses on hydraulic diameter (Dh = 4A/P, where A is duct area and P is duct perimeter) in order to establish a division between channel types according to their flow characteristics as follows.

- Conventional channels: $Dh > 3mm$
- Minichannels : $3mm \geq Dh > 200\mu m$
- Microchannels: $200\mu m \geq Dh > 10\mu m$
- Transitional Microchannels: $10\mu m \geq Dh > 1\mu m$
- Transitional Nanochannels: $1\mu m \geq Dh > 0.1\mu m$
- Molecular Nanochannels: $0.1\mu m \geq Dh$

Kandlikar [4, 5] states that the above criteria are created by focusing on gas flow where the mean free path of the fluid is significantly larger than liquids. Mean free

path of air (0.068 μm) is two orders of magnitude larger than the pure water's (0.00025 μm). Therefore, microscale heat transfer effects are an important concern for gaseous flows in microchannels. In one of the most extensive review papers on microchannels, Kandlikar and Grande [6] investigated the effect of hydraulic diameter on heat transfer and pressure drop. In Figure 1.1 [6], the relation between the heat transfer coefficient and hydraulic diameter is presented under constant heat flux boundary condition and the assumption of no rarefaction and compressibility effects. In Figure 1.2 [6], the variation of pressure gradient (pressure drop) with channel size is presented for fully developed laminar flow in smooth circular tubes at 300 K for water at 200 kg/m^{2}s (V= 0.20 m/s) and air at 5 kg/m^{2}s (V= 4.25 m/s) under the same assumptions of no rarefaction and compressibility effects)

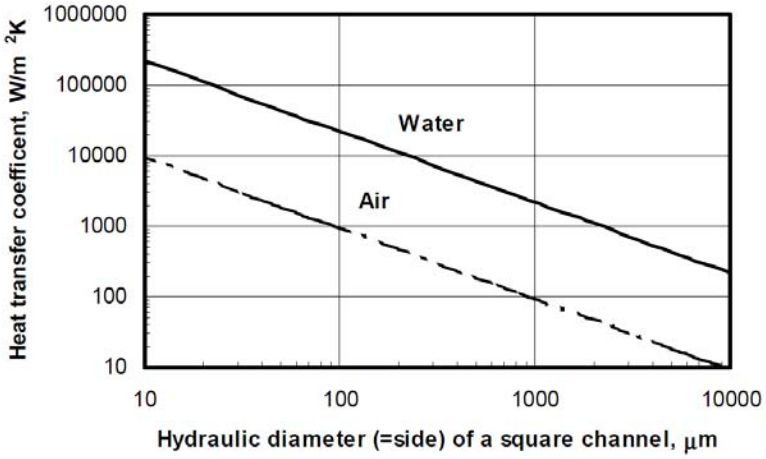

Figure 1.1: MDT process schematic [6]

It is clearly seen from Figure 1.1 and Figure 1.2 that a reduction in the channel size results in a tremendous enhancement in heat transfer coefficient and increase in pressure gradient at an even more dramatical rate.

An experimental study is conducted by Richter et al. [7] where triangular microchannels (54.7° side angles) with top width ranging between 28 μm to 182.7 μm with 2 mm length and are studied for 2 mm length of the flow channel. At flow rates in between 0.01 to 1000 μl/min, flow is determined to be laminar with Reynold number less than 1. The study compared experimental results with the predictions using standard channel friction factors and their agreement was almost perfect. In addition, the study conducted by Pfahler et al. on microchannels with a dimension between 135

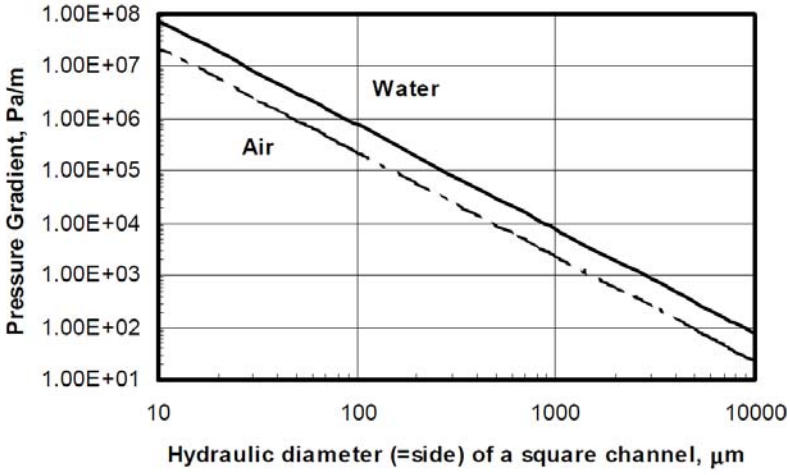

Figure 1.2: MDT process schematic [6]

µm to 0.8 µm concluded that the conventional fluid mechanics theory is applicable in microchannels with dimension as small as 1.7 µm.

Kandlikar and Grande [6] states that microchannels are at the infancy stage from a historical perspective. They expect that the widespread availability of microchannels will begin with the advances in MEMS devices and systems, microscale sensor and actuator, extreme heat flux removal systems and biomedical applications such as artificial kidneys or lungs for human implant. In this thesis, a thermal management design with microchannels for an electronic warfare system is studied. The author believes that the military systems can be included in the list of microchannel application areas due to requirements of advanced electronic performance (extreme heat fluxes) and environmental constraints. The heat removal capacity of microchannels is quite promising considering the published studies with extreme heat fluxes ranging between 1000 to 100000 W/cm^2 [8]. Although there is a numerous number of researches published on microchannels, it is seen that there is a gap in the literature on studies focusing on the effects of manufacturing errors of microchannel heat sinks.

1.2.2 Manufacturing Methods of liquid Cold Plate with Microchannels

The cold plates with embedded microchannel heat sink are generally produced as two parts which are joined later by different manufacturing techniques. There are sev-

eral manufacturing techniques to create the micron level dimensions of microchannels. The main manufacturing methods used in microchannel production are wire erosion, precision CNC, 3D metal printing and patented Micro Deformation Technology (MDT).

Wire erosion is a type of Electrical Discharge Machining (EDM). This technique invented by two Russian scientists in 1943, Butinzky and Lazarenko [9]. Their search on prevention of the erosion of tungsten due to sparking resulted with invention of the EDM technique. The EDM uses electrodes, dielectric liquid and voltage to erode and shape the material. Workpiece and cutting wire are the two electrodes which are placed in a dielectric liquid where they move relative to each other in order to create the shape needed. Wire electrode is never contacting the workpiece but rather it is surrounded by the dielectric liquid. Voltage and current are produced by the power supply to generate a spark. Spark erosion shapes the material by deforming and removing the unwanted portions. Dielectric liquid is also helps to cool of the electrodes while flushing the eroded particles. These particles are removed by a filtration system and liquid is used again [10]. Diameters of the wire range from 0.1 mm to 0.33mm and tolerances are about 0.005mm [11]. Oztoprak and Tarı published the paper titled "Microchannel Cold Plate Dimensional Precision Effects on Performance", in which the manufacturing inaccuracies of microchannels manufactured by EDM technique are investigated. The paper concludes that the dimensional imprecision of microchannels can improve cooling performance while causing an increase in pressure drop [12].

The precision CNC (Computer Numerical Control) is another manufacturing option for microchannels. CNC is computer-aided system that uses a tool (drill, laser etc.) to shape the material by discharging or cutting. There can be three to nine different axis tool paths in a CNC machine [13]. CNC machines can achieve tolerances around 0.12 mm, fine machining has tolerances around 0.025 mm and processes like lapping and polishing can offer tolerances of about 0.0013 mm. The ratio between the diameter and length of the tool is rather limited. Therefore, the high depth/width ratio required in microchannels can become a hard task for CNC machining. To summarize, it is very time-consuming to create microchannel fins with a CNC machine while final product quality is questionable, especially for dimensions under 0.5 mm.

3D printers are using additive manufacturing techniques. They create the final part by laying numerous material layers one on top of another. Unlike the 3D plastic printers, the 3D metal printers are using powder-based fusion using powdered metals with pieces as small as 10 microns. The 3D metal printer lays a layer of metal powder on the table and then it uses selective laser melting to fuse the material and create the intended shape. This technique has almost no limitations regarding the shape of the material, so it can create a much lighter part and also can produce shapes that cannot be created with any other technique. An important advantage of 3D printing techniques is the ability to create the cold plate as one part rather than two. Therefore, additional manufacturing processes of part joining can be omitted. 3D metal printing is a recent technology. Although it is gaining popularity, the technique has some disadvantages such as extremely long machining duration, high energy consumption, high investment costs, and most importantly low material density. Since the parts are produced out of by spherical powder pieces, the final part ends up with lower density (air gaps present within the part) which results in a decrease in thermal conductivity and degradation in strength. Including the limited availability in the market, the 3D metal printing technique needs further improvement to be used in microchannel manufacturing, especially in military systems [14].

Micro Deformation Technology is a patented technology that is used for microchannel production by the cold plate manufacturer MicroCool®. It uses a special tool to plastically deform ductile materials which are prepared for the process by pre-machining. The tool moves along the material and creates liquid channels by deforming and lifting the material as shown in Figure1.3 [15]. It can create very high fin densities up to 650 fins per inch (FPI) [16]. The MDT can be considered an innovative method for serial production of microchannels with improved cost efficiency and reduced production costs compared to more conventional approaches like chemical etching and wire EDM.

In this study, microchannels are produced by the patented Micro Deformation Technology. The two parts of microwave modules are joined by friction welding technique in aluminum modules and by brazing method in copper modules.

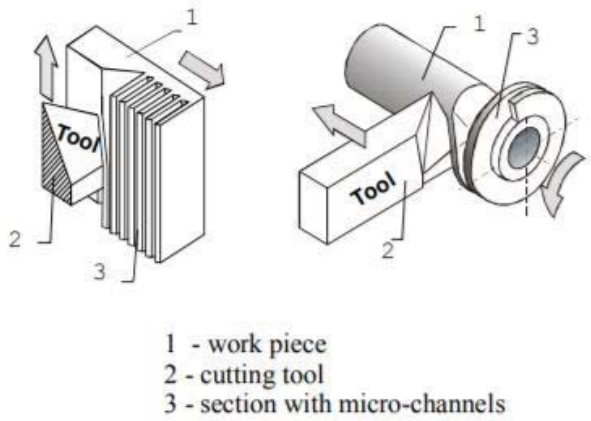

Figure 1.3: MDT process schematic

1.3 Overview of the Thesis

To achieve the objectives of this thesis, microwave modules are designed according to specific constraints. Afterward, numerical analyses conducted to investigate performance improvements. The modules are produced and tested in prepared experimental setup. Experimental results are analyzed and further numerical simulations are conducted to understand the effect of manufacturing inaccuracies. The results of the study are then compared and further analyzed. The overview of the thesis is as follows.

In Chapter 2, the thermal design and numerical analysis are presented with detailed thermal problem definition and conceptual design procedures. The CAD designs of the alternative microwave modules with microchannels are presented. Afterward, the numerical simulation model and the results of the simulation runs are presented and discussed.

In Chapter 3, the details of the experimental procedures and established experimental setup are presented. The experimental results are discussed where possible sources of discrepancies are investigated. The main source of these discrepancies is found to be the manufacturing inaccuracies in microchannels.

In Chapter 4, post-experiment analyses are presented where the effect of manufacturing errors and inaccuracies in microchannels are investigated.

In Chapter 5, the content of this study is summarized and concluding remarks are presented with suggestions for the future work to further extend this study.

CHAPTER 2

THERMAL DESIGN AND NUMERICAL ANALYSIS

In this chapter, the thermal design phase is discussed in detail resulting with the alternative microwave module designs and numerical simulations are presented and discussed. The author feels obligated to note that some parts of this chapter may also be related to a patent application filed by ASELSAN (Author's current employer) in which the author is named under contributors with a major percentage. All content of this chapter is created by authors sole work unless explicitly specified otherwise. It is also important to note that the unit containing the microwave modules with microchannels, is a critical component of a radar and electronic warfare system. Therefore, the specific details about the electronics and functional specifications are not presented and these details are not necessary for the scope of this study. This chapter starts with the definitions of the thermal problem and conceptual design, where the methods followed to establish a preliminary design are discussed in detail. The second part of the chapter presents the detailed mechanical design phase of microwave modules with selected design alternatives, numerical analyses of the established designs and discussions of the simulation results.

2.1 Definition of the Thermal Problem and Conceptual Design of Microwave Modules with Microchannels

The essence of thermal design challenges faced by the author is to achieve satisfactory cooling of high heat fluxed chips under strict volume constraints. The electronic warfare subsystem consists of several microwave modules containing several RF power

amplifier chips with extreme heat fluxes. The microwave module with power amplifier chips is presented in Figure 2.1. The module consists of three driver PA chips with heat dissipation of 5 W each and three main PA chips with 10 W of heat dissipation each. Total heat dissipation is 195 W. The size constraint regarding the microwave module dimensions is 125x45x25 mm. Considering the chip sizes are about 3x4.5 mm and the actual heat dissipation in a chip occurs in the transistor layout area of about 0.05x3 mm; it can be concluded that the thermal management solution for a continuous work (CW) application is challenging with traditional liquid cooling methods due to limited heat transfer area. The power amplifier thermal characteristics will be further discussed in Section 2.1.1. In order to overcome confidentiality concerns of the company, in this study power amplifier chips are replaced with diamond resistors in numerical analyses and experiments. The diamond resistors are selected so that they provide an almost perfect representation of the PA chips. To illustrate, an aluminum module with microchannels with 25 FPI fin density which is prepared for experiments is shown in Figure 2.2.

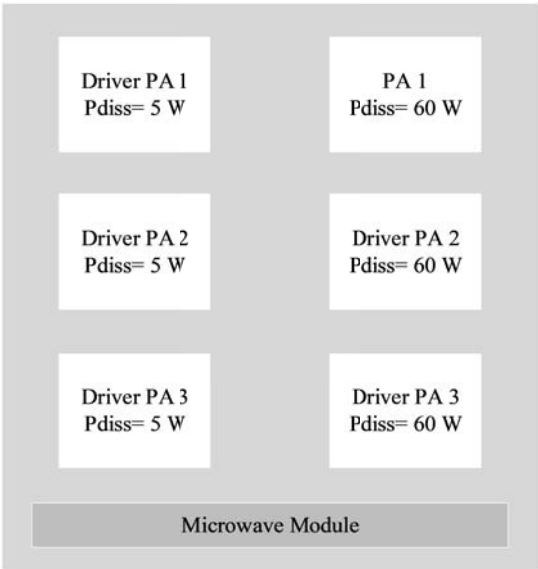

Figure 2.1: Microwave module layout

In conceptual design, keeping in mind the overall weight and volume limitations of the unit due to rotary platform integration requirements; the microwave modules are placed radially in an enclosure where the coolant is delivered and collected via radial manifolds. Although the manifolds are designed by the author through a combination of a detailed literature survey, numerical analysis, and experiments, leading to

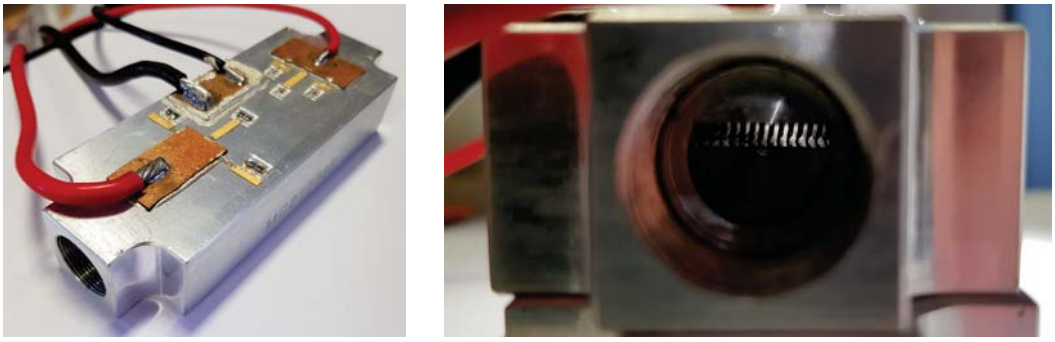

(a) (b)

Figure 2.2: Aluminum module with microchannels prepared for experiments (a) Isometric view (b) Front view in which the microchannel heat sink is visible

a uniform liquid distribution under the volume constraints, their design is out of the scope of this study. The actual number of microwave modules in the unit is also not of importance for this study. The basic overview of the overall thermal management structure of the unit is shown in Figure 2.3.

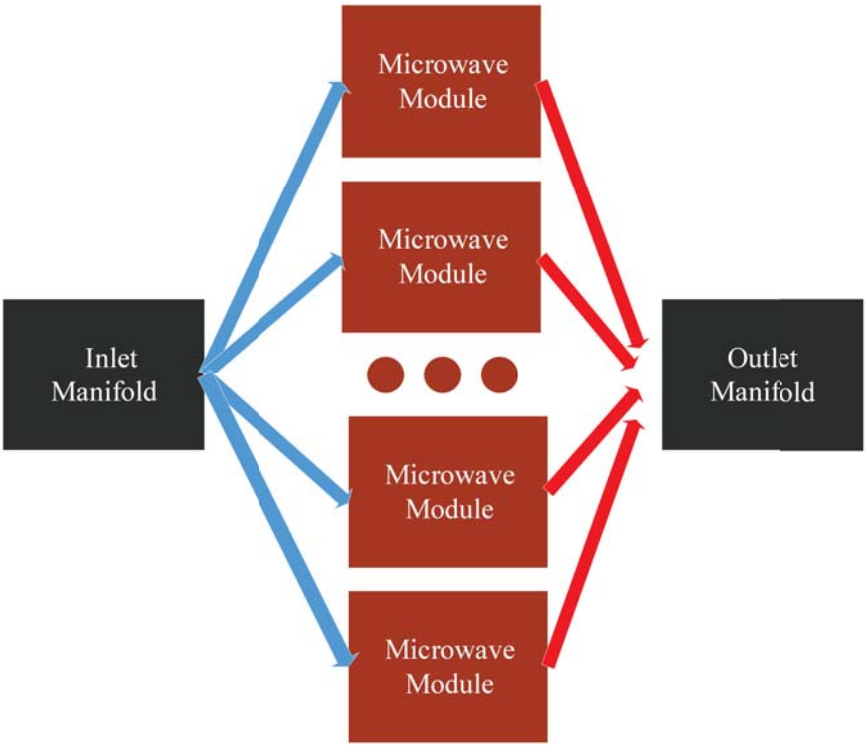

Figure 2.3: Basic overview of the overall thermal management structure of the unit

The focus of this study is the individual microwave modules with embedded mi-

crochannel liquid flow passages. The modules with microchannels are designed and manufactured with different fin densities and of different materials i.e. copper and aluminum. The manufacturing inaccuracies and defects in microchannels and their effect on thermo-fluid performance will be discussed further in Chapter 4.

2.1.1 Thermal Characteristics of Radio Frequency Power Amplifiers

The radio frequency power amplifier (RF PA) is an electronic amplifier used to convert a low-power RF signal into a signal with a higher power. An RF designer must consider the following design parameters for successful functionality: gain, power output, bandwidth, power efficiency, linearity, impedance matching and heat dissipation [17]. In this study, the focus is on thermal characteristics and heat dissipation of the RF PA, therefore duty cycle (DC), pulse width (PW) and bandwidth frequency of the chip are not discussed. There are two main types of RF PAs: solid state devices such as MOSFETs (metal-oxide-semiconductor-field-effect transistor) and vacuum tube amplifiers [17] A MOSFET (metal-oxide-semiconductor field-effect transistor) type RF PA is used in this study.

The microwave module used in this study contains gallium-nitride on silicon carbide power amplifiers (GaN on SiC HEMT) due to their better thermal properties and high-temperature reliability. The older gallium-arsenide (GaAs) based PA chips had lower limiting junction temperature values of 175 °C, compared to 275 °C of GaN-based PA chips. In addition, GaN chips provide much better heat transport with more than three times higher thermal conductivity (the thermal conductivity of GaN is about 1.7 W/cm-K, while the thermal conductivity of GaAs is about 0.46 W/cm-K) [18]. It should be noted that the thermal conductivity of materials such as silicon, GaN, GaS, AlGaN are temperature dependent and they should be modeled accordingly for accurate numerical simulations at the transistor level [19].

Designing a successful microwave module depends on understanding the stack-up layout and thermal characteristics of PA chips. An illustrative case is presented to explain the thermal design considerations using an arbitrarily selected GaN-based PA chip, TGF2023-2-10 from Qorvo. All related data of PA chip TGF2023-2-10 is taken from the manufacturer's datasheet [20].

The chip dimensions are 0.82x2.48x0.1 mm and the chip can dissipate up to 40 W. Without specifying the heat source further at the transistor locations, heat flux can be found as follows:

$$q''_{PA} = \frac{P_{diss}}{Area} = \frac{40W}{0.82x2.48mm^2} = 19,67\frac{W}{mm^2} \tag{2.1}$$

It is also imperative that the thermal characteristics of PA chips significantly depend on the heat dissipation rates as seen shown in Figure 2.4. The rate of heat dissipation affects the thermal resistance between chip junction temperature and baseplate temperature. The most important objective of thermal management design is to keep the junction temperatures low. The junction temperature value determines the mean lifetime of the PA chip while also affecting the power efficiency of the chip.

Parameter	Test Conditions	Value	Units
Thermal Resistance, θ_{JC}	P_D = 10 W, Tbaseplate = 85°C	4.1	°C/W
Channel Temperature, T_{CH}		126	°C
Median Lifetime, T_M		4.3E10	Hrs
Thermal Resistance, θ_{JC}	P_D = 20 W, Tbaseplate = 70°C	4.5	°C/W
Channel Temperature, T_{CH}		174	°C
Median Lifetime, T_M		1.9E8	Hrs
Thermal Resistance, θ_{JC}	P_D = 30 W, Tbaseplate = 85°C	5.0	°C/W
Channel Temperature, T_{CH}		236	°C
Median Lifetime, T_M		7.6E5	Hrs
Thermal Resistance, θ_{JC}	P_D = 40 W, Tbaseplate = 85°C	5.6	°C/W
Channel Temperature, T_{CH}		310	°C
Median Lifetime, T_M		4.6E3	Hrs

Notes:
1. Assumes eutectic attach using 1.5 mil thick 80/20 AuSn mounted to a 10 mm x 10 mm x 40 mil CuMo Carrier Plate.

Figure 2.4: TGF2023-2-10 Mean Lifetime and Thermal Resistances with respect to Heat Dissipation and Base Plate Temperature under Continuous Work (CW)

The relation between the mean lifetime and the junction temperature are presented in Figure 2.5 TGF2023-2-10. In the plot, the lifetime varies logarithmically; therefore a 25 °C increase in junction temperature results in 10 times decrease in the mean lifetime.

In military systems, reliability is of vital importance. Even though most systems have a guarantee period of 5 years, a designer must consider a significant safety margin in order to account for extreme operating conditions of military equipment. Therefore, it was determined that the PA chip junction temperature should be kept under 250°C and the design objective is to keep this value as low as possible in order to achieve a

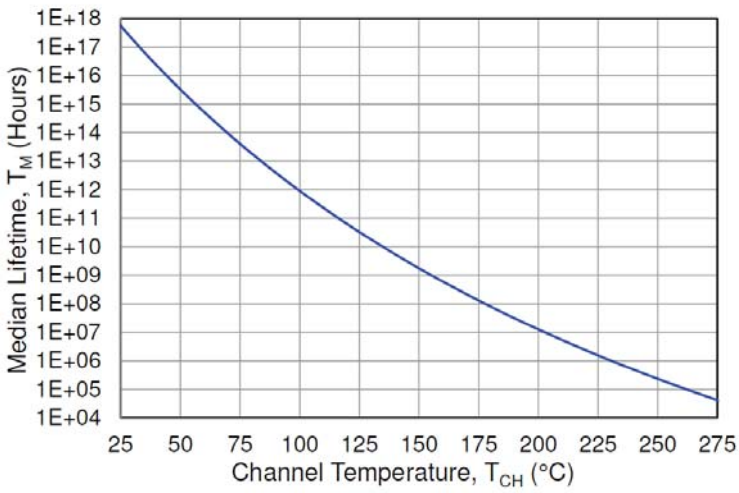

Figure 2.5: Mean lifetime vs channel temperature

better safety margin. It should also be noted that the temperature-based failures of PA chips mostly start from a single transistor located at the center. As a rule of thumb, the transistors located in the center experience the highest temperature values and when one transistor fails or burns-out; other transistors become overloaded by means of received electrical and RF power per transistor. In conclusion, the functional failure of a single transistor dissipating heat in an area of about 50 nanometers to 100 microns can lead to complete PA chip failure by creating a domino effect. An infrared camera image of the transistor region of a GaN PA chip is shown in Figure 2.6 [21]. The heat dissipation area at transistor level has a vertical length of 50 nm [22] to 500 nm [23].

The experimental measurement techniques such as infrared cameras, liquid crystal thermography, micro-Raman thermography, photoluminescence and transient thermo-reflectance help PA chip manufacturers in the thermal characterization of chips [24]. Even though these techniques based on state-of-the-art methods; they have high investment costs and limited accuracies due to temperature resolution levels [24]. Micro-Raman thermography offers possibly the best thermal resolution by providing spatial, temporal, and thermal resolutions of 0.5 µm, 10 ns, and ±5 K [25]. Even though the resolution of the micro-Raman method is remarkable, the extremely small size of transistor-level heat dissipation area can cause inaccuracies. The RF PA chip users may want to test chips under their specific operating conditions but these types of experiments are unlikely to be conducted due to the aforementioned difficulties.

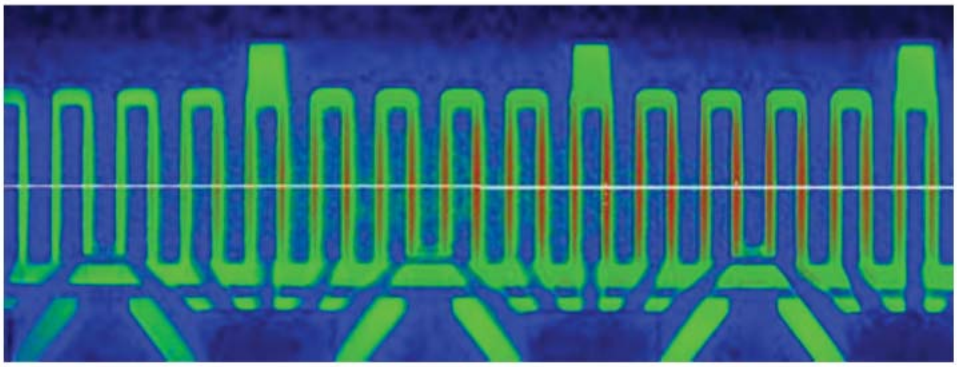

Figure 2.6: An infrared camera image of the transistor region of a GaN PA chip

Oztoprak and Erkek published the paper [19] titled "Thermal Performance Improvement of an Air-cooled GaN-based Solid State Power Amplifiers", in which the necessity of careful modeling for accurate junction temperature estimation of a PA chip is stated. In addition, thermal characteristics to be observed in material selection for mechanics and PA chip interface are investigated. The paper concludes that an order of magnitude increase in PA chip lifetime can be achieved by selecting module material of pure copper instead of aluminum 6061 and high thermal conductivity epoxy instead of indium foil [19].

In this study, the aforementioned precautions are taken in order to achieve the best thermal solution for chip connection. The interface is kept simple by means of avoiding the additional carrier plates, chip packaging mechanics and the epoxy/solder layers. A typical thermal stack-up is shown in Figure 2.7 [26]. The typical stack-up has the following features introducing thermal resistances; two mechanical layers, one epoxy layer and a metal/composite-to-metal thermal contact resistance between the carrier and the metal housing. To avoid these additional thermal resistance, the heat flow from the PA Chip to the cooling liquid is designed for the best thermal performance under limitations of current manufacturing technology and material science as shown in Figure 2.8. The major disadvantage of the refined stack-up is to overcome the coefficient of thermal expansion (CTE) mismatch between the PA chip substrate, silicon carbide and module material of aluminum or copper. This problem is avoided by using a high thermal conductivity flexible epoxy (SK70N from Namics Corporation), with a slight decrease in thermal conductivity of 50 W/m^{2}K compared to Au80Sn20 eutectic solder with 57 W/m^{2}K. In addition, a better flatness accuracy

of the module mechanic is needed for microwave process requirements. Another requirement of this stack-up is that the RF components which are placed on the module in a clean room environment via established processes need careful handling by technicians leading to longer process durations.

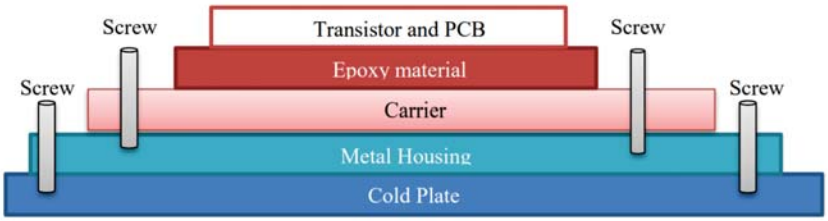

Figure 2.7: Typical thermal stack-up of a PA chip and microwave module

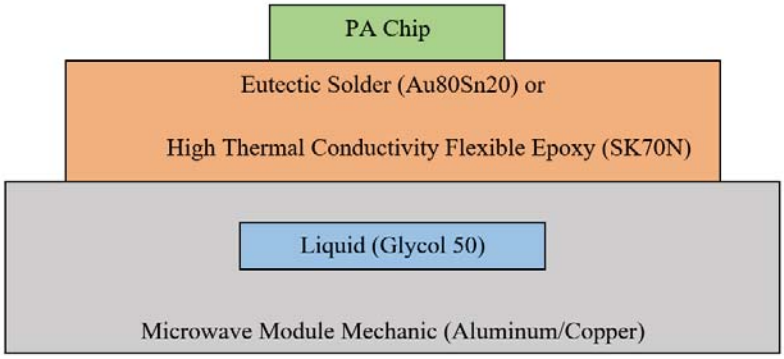

Figure 2.8: Stack-up of the PA chip and microwave module with liquid cooling

The focus of this study is to investigate the applicability and validity of single phase microchannel liquid cooling for a microwave module with power amplifiers considering the thermo-fluid performance of microchannels. The RF PA chips are replaced by diamond resistors with high-temperature durability while keeping the stack-up structure the same. Since the objective is to achieve the lowest junction temperature for a PA chip with the constraint of 250 °C, the resistor mock-up will serve as an investigation medium to understand the effect of microchannel dimensions and material selection on temperature distribution. For this purpose, a predetermined thermal resistance value between the module's surface temperature and the junction temperature of the chip will be used. The author feels obligated to once again note that the overall design product in which these microwave modules are embedded is a novel design and a patent application was filed to protect its trademark value. Therefore, specifi-

cations related to RF electronics are not shared including the exact PA chip type and brand. This will not affect the content of this study in any way. The PA chip thermal characteristics will not be further discussed. The diamond resistors are selected to simulate the high dissipated heat fluxes of PA chips. The junction temperature of the PA chip is estimated using the surface temperature of the module in contact with the diamond resistors. Using the obtained surface temperature from numerical simulations and the junction-to-case thermal resistance value given by the manufacturer (the resistance value also accounts for the eutectic solder layer between the chip and module surface), the junction temperature of the PA chip is estimated.

2.1.2 Diamond Resistors

The diamond resistors are used as the replacements of PA chips to achieve low experimental costs and to avoid exposure of microwave electronics. The exact description of diamond resistors stated by manufacturer EMC Technology is "CVD Diamond Chip Resistor". The diamond resistors are selected according to their compact size, ability to provide high heat fluxes and their high operating temperature limits of up to 150 °C. It is important to note that the rated power of the resistors (directly correlated with heat dissipation rate) decays significantly with increasing temperature as shown in Figure 2.9 [27]. Therefore, the heat dissipation rate of the resistors should be carefully monitored for temperatures above 125 °C by power supply unit readings.

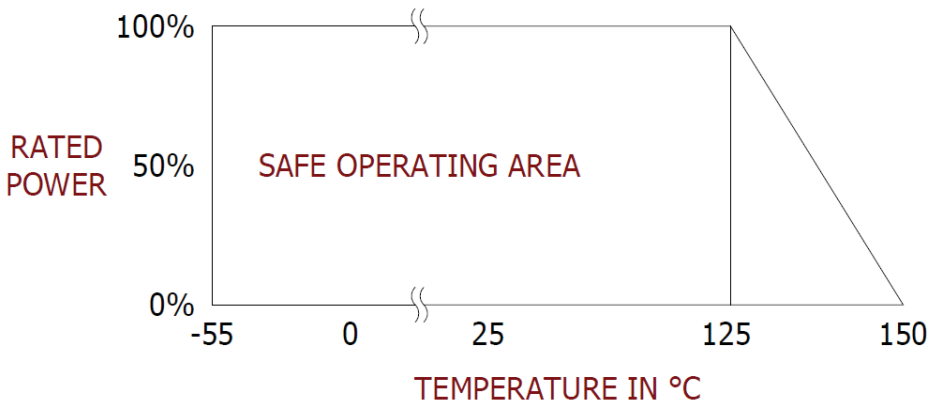

Figure 2.9: Rated power of CVD diamond chip resistor vs temperature

Driver PA chip and main PA chip are replaced by different diamond resistors due to their different sizes and heat fluxes. Driver PA chips dissipate a rather low power of 5

W, compared to 60 W power dissipation of the main PA chip. The driver PA chips are simulated by "CVD Diamond Chip Resistor 20 Watts", with part number CR0402D. The datasheet and the dimensions of the resistor are presented in Figure 2.10 [27]. The resistor will dissipate 5 W when it is supplied with an electrical power of 0.316 Amperes at 15.81 Volts.

ELECTRICAL

Resistance:	50 Ω & 100 Ω, ± 5%
Frequency Range:	DC – 30 GHz
Capacitance:	0.09 pF Typical
Input Power CW:	20 Watts
Peak Power:	200 Watts (1 μs pulse width/1% duty cycle)

ENVIRONMENTAL

Operating Temperature:	-55°C to +150°C
Storage Temperature:	-55°C to +150°C

MECHANICAL

Substrate Material:	CVD Diamond
Resistive Element:	Thin Film
Terminal:	Gold over Nickel
Ground Plane Material:	Gold over Platinum

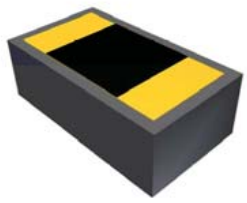

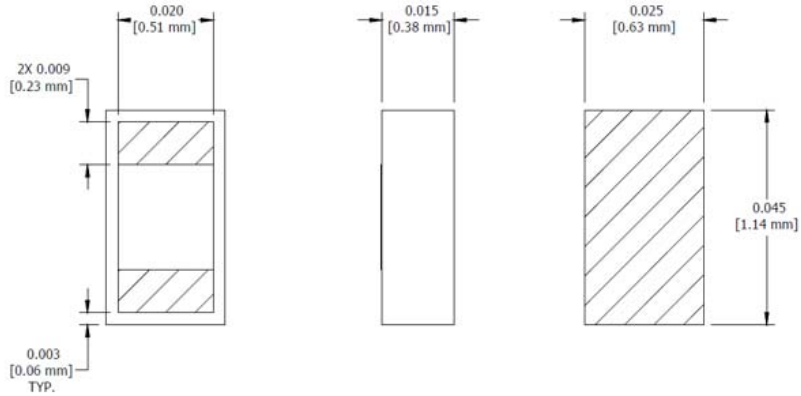

Figure 2.10: Overview of CVD Diamond Chip Resistor 20 Watts

Each main PA chip is simulated with two diamond resistors in accordance with the PA chip's dimensions and heat flux. The replacement diamond resistors for the main PA chips are titled "CVD Diamond Chip Resistor 50 Watts", with part number CT0505D. The datasheet and the dimensions of the component are shown in Figure 2.11 [28]. Each diamond resistor dissipates 30 W, achieving a total of 60 W at each main PA chip location. In order to simulate PA chip dimensions, the diamond resistors are placed one on top of the other with 1 mm distance between them. Each resistor is

expected to dissipate 30 W when it is supplied an electrical power of 0.775 Amperes at 38,73 Volts.

ELECTRICAL

Nominal Impedance:	50 Ω ± 5%
Frequency Range:	DC – 20 GHz
Input Power CW:	50 Watts
Peak Power:	500 Watts (1 µs pulse width/1% duty cycle)
VSWR:	1.6:1 Max

ENVIRONMENTAL

Operating Temperature:	-55 °C To +150 °C
Storage Temperature:	-55 °C To +150 °C
Temperature Coefficient:	±200 PPM/°C Max

MECHANICAL

Substrate Material:	CVD Diamond
Terminal Material:	Gold over Nickel
Ground Plane Material:	Gold over Platinum
Resistive Element:	Thin Film

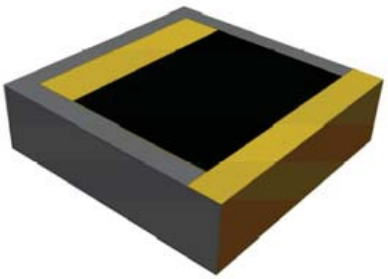

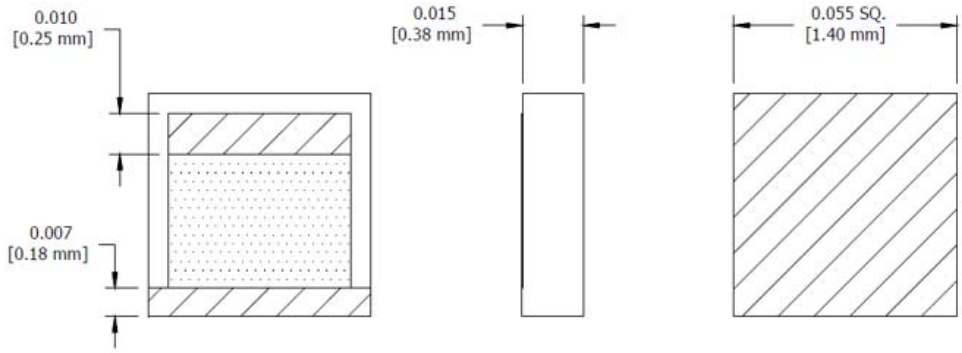

Figure 2.11: Overview of CVD Diamond Chip Resistor 50 Watts

The diamond resistors provide close resemblance to PA chip as a heat source with acceptable accuracy. Determining their type and dimensions is necessary to continue with the mechanical design of the microwave module.

2.1.3 Conceptual Mechanical and Thermal Design of Microwave Module with Microchannels

The mechanical design of the microwave module is far from being flexible due to strict requirements of size, shape and mass. The unit containing microwave modules is to be placed on a rotary platform inside a protective enclosure (radome). The di-

mension restrictions are determined so that the microwave module volume stay inside the envelope of 125x45x25 mm while aiming for the smallest volume possible. Another important input for mechanical design is the pattern of microwave electronics. The pattern is usually determined by the RF design engineer and later the mechanical design is completed accordingly. In our case, an iterative design process is performed to achieve the optimal thermal and electronic design.

2.1.3.1 PA Chip Locations (Pattern of Microwave Electronics Design)

The main function of a PA chip is to amplify RF power. In the presence of several PA chips in a microwave module, in general, the RF signal is divided in accordance with a number of PA chips and after amplification at the PA chips, the signals combined with microstrip lines on the module face. The length of microstrip lines is important since they cause attenuation in the RF signal, especially for amplified RF signals. Therefore, keeping microstrip lines between PA Chips shorter is crucial to achieve the aimed signal amplification. Another important design requirement is that the microstrip lines leaving each PA chip to combining point should have precisely the same length to avoid any phase and amplitude changes between RF signals. In our case, three microstrip lines leaving the three main PA chips are to be joined at the combining point. The length of these three microstrip lines should be as short as possible for signal attenuations while keeping their length equal.

On the other hand, a thermal design should avoid dense placement of high power dissipated heat sources to avoid temperature increase from overlapping heat spreading. In other words, there is an obvious contradiction between thermal and microwave electronics design constraints. An optimal design can only be achieved by an iterative study between two disciplines. The PA chips should be located as distant as possible from each other to achieve lower junction temperature without making microstrip lines longer. After initial discussions, the optimal layout instinctively found in triangular placement as so-called “separate triangles pattern” as shown in Figure 2.12. The exact dimensions determined according to RF signal behavior in microstrip lines and signal characteristics introduced by 90° turn (L_{turn}) in an iterative manner. The details of RF signal characteristics and microwave pattern design methods followed

are out of the scope of this study.

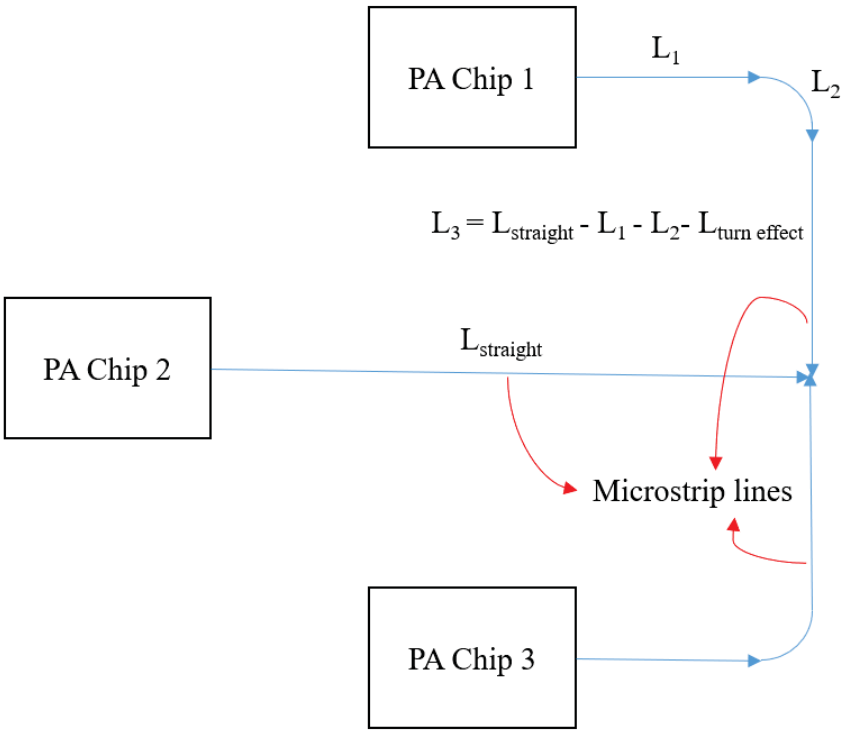

Figure 2.12: PA placement on microwave module with "seperate triangles layout "

2.1.3.2 Conceptual Design of Microwave Module with Microchannels

To start the conceptual design phase, it is imperative to determine design parameters and categorize them by their flexibility. The design parameters which are predetermined by system requirements are presented in Table 2.1. In military systems with liquid cooling, the liquid is delivered to the system by a so-called “liquid control unit” and the inlet temperatures are generally 35 °C or above. The liquid inlet temperature of a system to be cooled depends on many factors such as the solar load on hoses, characteristics of the liquid control unit (pumping rate, heat exchanger type, the presence of refrigeration cycle, the distance between the supply and cooling system), the ambient temperature and the type of liquid. The temperature of the liquid at the microwave module inlet is determined to be 25 °C in order to keep inlet temperature fluctuations at a minimum in the experiments. The inlet temperature can be adjusted later for a specific value once the numerical CFD model is established. In this study, the liquid (coolant) selected as glycol50 (a mixture of 50% pure water and 50% ethy-

lene glycol) considering its availability in wide-range of land and naval platforms. The liquid flow rate is also predetermined as 2 lpm (liters per minute) considering the number of modules in the unit and liquid supply capacity of the available liquid control unit.

Table 2.1: Predetermined design parameters

Parameter Definition	**Parameter Description**
Cooling liquid type	Glycol 50
Height	25 mm
Width	45 mm
Depth	125 mm
Liquid flow rate	2 lpm

Since the size requirements combined with material selection determines weight, it is limited by the density of module material. A module produced from materials with a density up to 9.5 g/cm^3 safely stays within weight requirement including the weight of liquid filling internal cavity. Therefore, almost all traditional manufacturing metals stay within the margins including pure copper with a density of 8.933 g/cm^3. For the design parameters that are flexible, the objective is to achieve the minimum junction temperature of the mounted PA chip. To achieve this objective, the author feels obligated to explore, test and evaluate the feasibility of all possible alternatives as all designers should. Considering the project schedule and the duration of this academic study; two product attributes to be varied are selected as the material and the fin density. The logic behind this selection is to establish alternative design solutions by varying the parameters with the highest impact on objective performance criteria. The module material alternatives are determined as aluminum and copper due to their availability, machinability, compatibility with chip mounting and microwave pattern installation processes and most importantly due to their high thermal conductivity. In the authors 6 years engineering experience with CNC machining and cold plates, two different fin densities are determined in order to evaluate the dimension of liquid channels' effect the on cooling performance. Considering the commercial value of the overall product and an order of magnitude higher costs of electronic components compared to the module; material and machining costs of microwave module is rather

insignificant. Even though manufacturing costs can be discarded, the ability to manufacture locally is strongly preferred in military applications. It is also known to Author that in case of forced convection single-phase liquid cooling; with smaller liquid channels and solid fins, cooling performance improves. For achieving minimum chip junction temperature; the aim is to explore the performance improvement achieved by the smallest channel dimension, in other words, microchannels. The thermal performance improvement achievable by higher fin densities investigated by evaluating two alternative microchannel designs; first with 25 FPI (fin per inch) fin density and second with 85 FPI (fin per inch) fin density. The first alternative with 25 FPI fin density is selected according to local manufacturing preference with dimensions of 0.5 mm liquid channel width and 0.5 mm solid fin width. For the second alternative with 85 FPI fin density, the author contacted leading international thermal management and cold plate manufacturers such as AAVID, Thermocore, and Microcool. After several discussions with manufacturers; 85 FPI fin density is selected according to machinability from selected materials of aluminum and copper, the ability for serial production, ability to withstand the military standard impermeability test with 10 bar pressure. The flexible design parameters and constituting alternative module designs are presented in Table 2.2. In conclusion of conceptual design phase; four alternative microwave module with embedded microchannels are selected.

Table 2.2: Design alternatives and flexible design parameters

Design Alternatives	**Material of Microwave Module**	**Microchannel Fin Density (FPI, fin per inch)**
Module 1	Aluminum	25
Module 2	Aluminum	85
Module 3	Copper	25
Module 4	Copper	85

Further considerations such as feasibility and power efficiency of the pump supplying the liquid with necessary pressure and flow rate; and availability of a slip ring with required specifications (in case of rotary platform integration) are to be determined in the final commercial product.

2.2 Mechanical Design of Microwave Modules with Microchannels

Detailed mechanical design of alternative microwave modules are to be done considering the prototype production and manufacturing limitations. The manufacturing method used in such plate designs produces two separate mechanical parts by machining all internal features of liquid passages and fins on them; then two parts are joined by methods such as brazing or friction welding. The solid fins of microchannels are machined on one part of the module by using various manufacturing methods as discussed in Chapter1. It is also important to note that even though the spatial envelope restrictions are determined, objective is to keep the module as small as possible.

Another important design decision for detailed design is to determine the type of liquid connectors (also named as "quick connects"). The mechanical interface between module mechanic and connectors contributes significantly to the height and shape determination of the module. The aforementioned unit constituting several microwave modules between inlet and outlet manifolds; encapsulates numerous electronic components in a very dense and compact manner. Therefore, the liquid connectors need to satisfy the requirements of blind mate, non-spill in case of opened connection and compensation of misalignment to comply with manifold manufacturing tolerances. The microwave modules connected to manifolds via liquid connectors are actually held in the air by these connectors. The connectors are selected as CGD-05 type quick connects from Stäubli company due to their compact size, advanced non-spill/non-drip safety features and high compensation for misalignment up to 1 mm between axes [29]. The connector interface threads are to be machined at both ends of modules. The conceptual design alternatives are detailed with CAD models according to manufacturing capabilities of the manufacturer.

2.2.1 CAD Design of Microwave Modules with Microchannels

In light of all design decisions, overall CAD models are created in coordination with the manufacturer. The manufacturer had applied different manufacturing techniques for different module materials of copper and aluminum which resulted in a slightly different mechanical design for the modules with different materials.

The part substituting microchannel fins are produced with manufacturer's patented "Micro Deformation Technology" (MDT) [15]. The main specifications of the process as follows [16];

- Fins per inch: 650 –5 (255-2 Fins/Centimeter)
- Fin Thickness to fin gap ratio: 1:0.2 – 1:3 (1:1 is typical)
- Fin height to fin thickness ratio up to 15:1
- Max fin gap: 2.5 mm for straight fins and 1.2 mm + for pins
- Pins can be formed in either an in-line or staggered pattern
- Pin diameter and gap vary from 1 mm to 0.5 mm
- Pin height to diameter ratio up to 8:1

The MDT process can be performed on materials such as titanium, stainless steel, silver, aluminum, copper and non-metallic materials like Teflon, polyethylene, rubber and PVC [16]. Example fin structures manufactured by MDT technique are presented in Figure 2.13 [16].

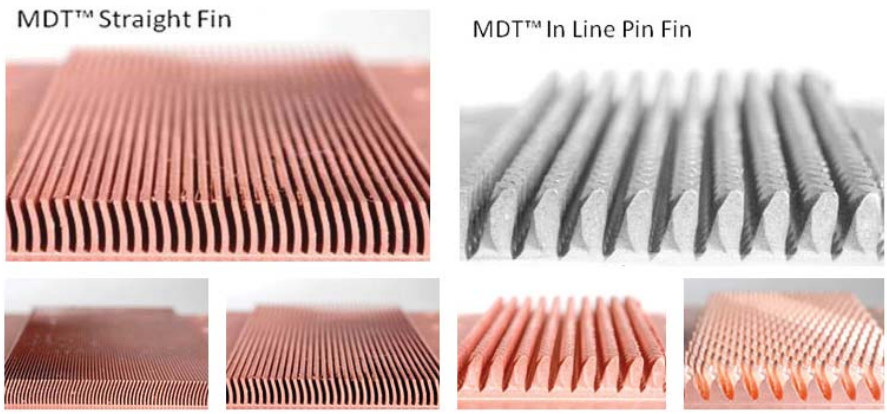

Figure 2.13: Example fin structures of MicroCool® Micro Deformation Technology (MDT)

2.2.1.1 CAD Design of Aluminum Modules

The CAD designs of microwave modules are created in light of all manufacturing and design considerations for an optimal solution. Aiming for the smallest possible

module, the microwave modules are determined to have outer dimensions of 110 mm (depth) x 20 mm (height) x 40.15 mm (width). Heat sources are placed on top of the module where 7 mm distance present between the heat source and the top surface of the liquid passage.

In aluminum modules, the two module parts are united by friction welding technique. Friction welding technique enables different connection lines comparing to the flat plane requirement of brazing (this is also possible with 3D vacuum brazing). Aluminum alloys have a wide range of thermal and mechanical characteristics according to their composition and post processes. The alloy decision is made according to the high thermal conductivity required for the part with microchannels and high stiffness and durability for the base part. Therefore, the module part with microchannels is produced from Al 1100 (with a thermal conductivity of 218 W/m-K) and module base is produced from Al 6061-T6 (with a thermal conductivity of 167 W/m-K) [30]. By combining all aforementioned design inputs, CAD model of aluminum modules with microchannels are created for fin densities of 25 FPI and 85 FPI accordingly. Detailed dimensions and technical drawings are not to be presented due to confidentiality concerns of both Aselsan and the manufacturing company. The CAD design of aluminum module with 25 FPI fin density, is presented in Figure 2.14. In Figure 2.14, it is shown that the two parts are united by friction welding along the welding surface with 360°coverage.

The 3D model of the aluminum module with two parts united is shown in Figure 2.15. The liquid channel height is 2.9 mm for 25 FPI in aluminum modules and the channel is not symmetrical. The channel position is determined by manufacturing limitations and thermal performance concerns, so that, the liquid passage within the module is slightly (about 3.1 mm) closer to the heat sources (top surface). By decreasing distance between heat sources and liquid flowing within the microchannel, the thermal resistance of the module (in which the heat transfer occurs due to conduction) can be reduced accordingly.

For different fin densities; aluminum modules differ in dimension due to the differences between the microchannel dimensions of width and height. The fin dimensions of aluminum modules are presented in Figure 2.16. Due to manufacturing limitations,

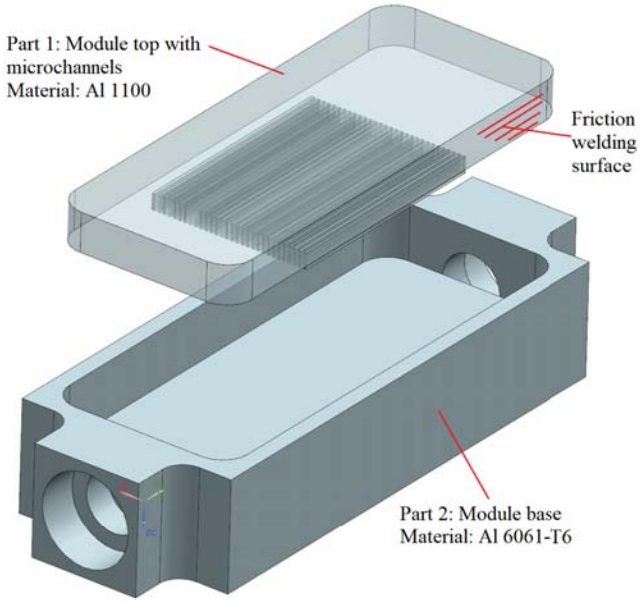

Figure 2.14: Aluminum module with two parts

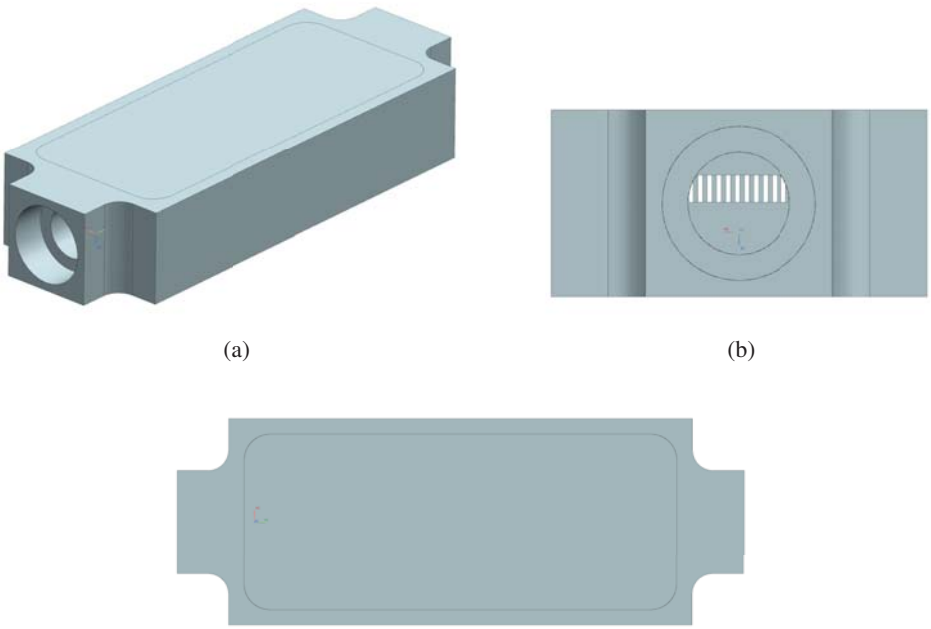

Figure 2.15: Aluminum microwave module with 25 FPI fin density after two parts united (a) Isometric view (b) Front view (c) Top view

fin height decreases with increasing fin density. Other than differences in height and width, the fin structure is the same in both modules where the fin surface area is 40 mm x 30 mm located at the longitudinal and lateral center of the module.

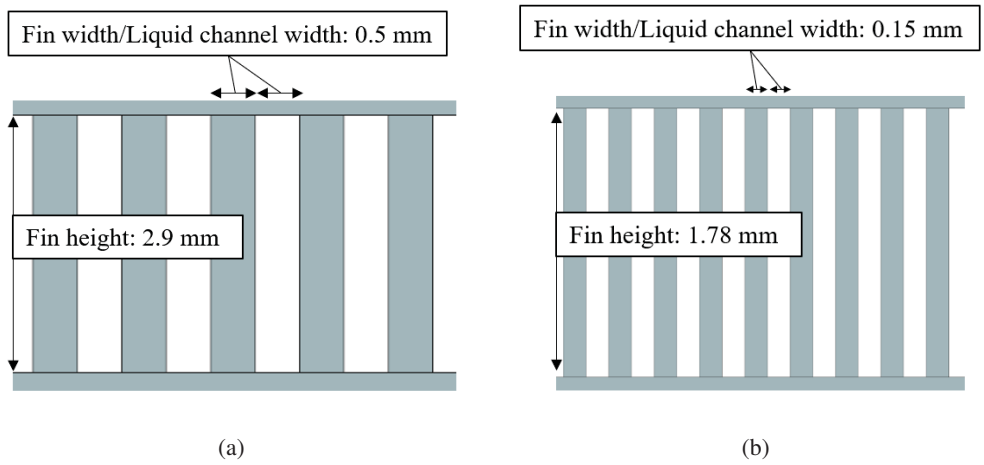

Figure 2.16: Microchannel fin dimensions of aluminum modules with different fin densities (a) 25 FPI fin density (b) 85 FPI fin density

2.2.1.2 CAD Design of Copper Modules

In pure copper modules, the two module parts are united by brazing technique. Brazing method requires flat surfaces to be joined, therefore the geometries of module parts differ significantly from aluminum modules. The module parts produced from pure copper with thermal conductivity of 387.6 W/m-K [30]. By combining all aforementioned design inputs, CAD model of copper modules with microchannels are created for fin densities of 25 FPI and 85 FPI accordingly. The CAD design of copper module with 25 FPI fin density, is presented in Figure 2.17 where the brazing surface is highlighted.

The 3D model of post manufacturing state of copper are shown in Figure 2.19. The liquid channel height is 5 mm for 25 FPI in copper modules and the channel is not symmetrical. The channel position is determined by manufacturing limitations and thermal performance concerns, as in the case of aluminum modules, the liquid passage within the module is 3.1 mm closer to the heat sources (top surface).

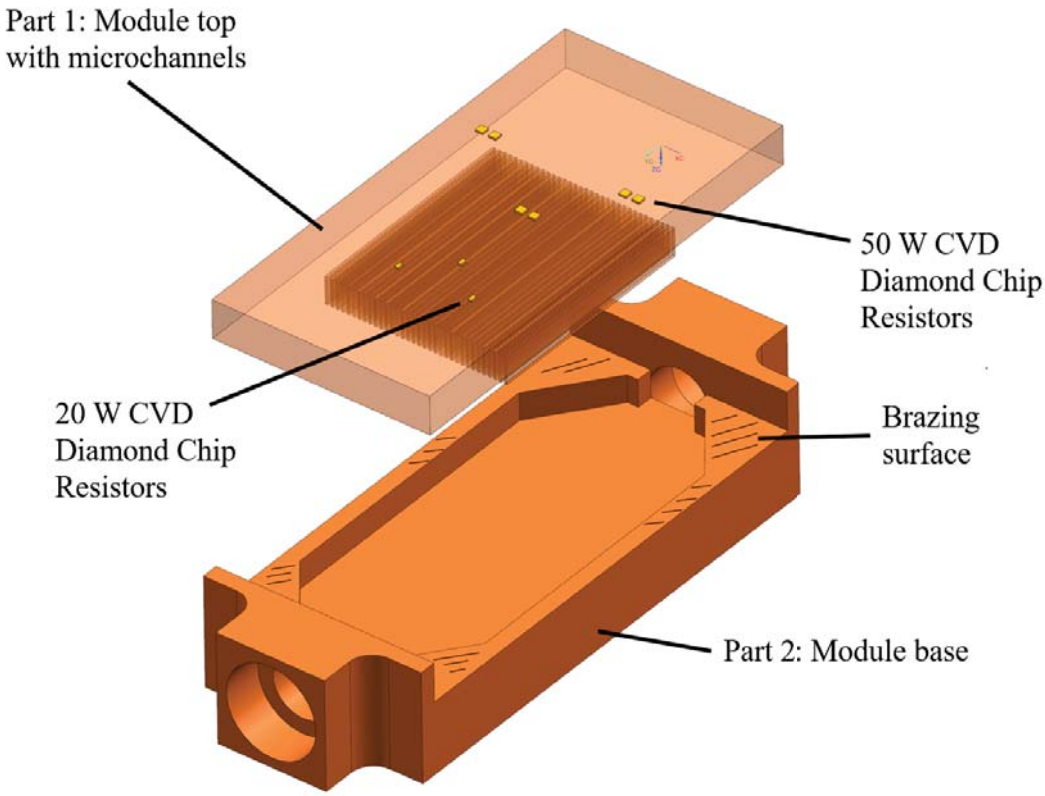

Figure 2.17: Copper module with two parts

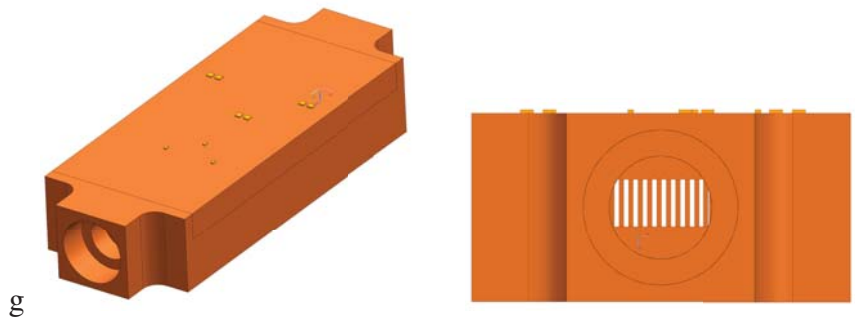

g

(a) (b)

Figure 2.18: Copper microwave module with 25 FPI fin density after two parts united (a) Isometric view (b) Front view

The fin dimensions of copper modules with different fin densities are shown in Figure 2.20. Due to manufacturing limitations, fin height decreases with increasing fin density. Other than differences in height and width, the fin structure is the same in both modules where the fin surface area is 40 mm x 34 mm located at the longitu-

dinal and lateral center of the module. The fin layout area in copper modules is 3 mm wider compared to aluminum modules due to brazing technique applied in copper modules. Moreover, with the copper material selection, module weight increases substantially. The copper microwave modules weighing 620 gr are 3.33 times heavier than aluminum ones weighing 186 gr. Considering the overall design objective of low weight, copper modules should provide a noteworthy cooling performance increase in order to be selected in the final design.

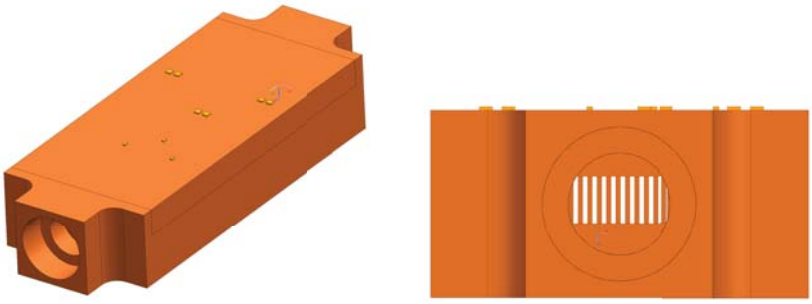

(a) (b)

Figure 2.19: Copper microwave module with 25 FPI fin density after two parts united (a) Isometric view (b) Front view

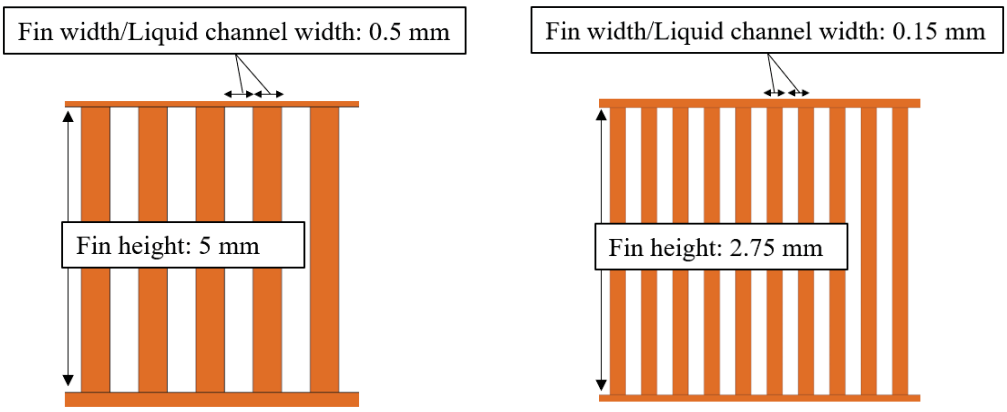

(a) (b)

Figure 2.20: Microchannel fin dimensions of copper modules with different fin densities (a) 25 FPI fin density (b) 85 FPI fin density

2.2.2 Overview of Alternative Designs

To summarize, four alternative microwave module designs established to explore their cooling performances. The alternative designs are identified according to their specifications in Table 2.3. The objective of alternative designs is to interpret the influence of material selection and fin density on thermo-fluid characteristics. Manufacturing limitations causes some unintentional variations in fin dimensions such as fin height and overall fin area. These variations provide an opportunity to evaluate the channel shape effect on cooling performance of microchannels.

Table 2.3: Specification of alternative designs

Module	**Module Material**	**FPI**	**Fin and Channel Width (mm)**	**Fin Height (mm)**	**Finned Area (mm x mm)**
Module 1	Aluminum	25	0.5	2.9	40 x 30
Module 2	Aluminum	85	0.15	1.78	40 x 30
Module 3	Copper	25	0.5	5	40 x 34
Module 4	Copper	85	0.15	2.75	40 x 34

2.3 Numerical Simulations of Design Alternatives

The established microwave module designs are evaluated by numerical simulations prior to experiments. Numerical simulations are conducted in ANSYS Icepak (release 19) software package which provides necessary modeling tools for heat transfer and liquid flow. The simulation model is to calculate an accurate estimation of physical phenomena happening during the microwave module operation. These physical phenomena are conduction in solid microwave module, fluid/liquid interaction at wet surfaces (in convection boundary layer), fluid flow from the inlet to outlet and conduction in the fluid.

2.3.1 Investigation on Simulation Run Speed

Prior to actual numerical simulation runs, a simple simulation model containing both heat transfer and liquid flow is created to investigate the calculation speed of Icepak software. The simulation model is presented in Figure 2.21.The mesh network consists of about one million elements and meshing process takes about 60 seconds with concurrency enabled for six CPU cores.

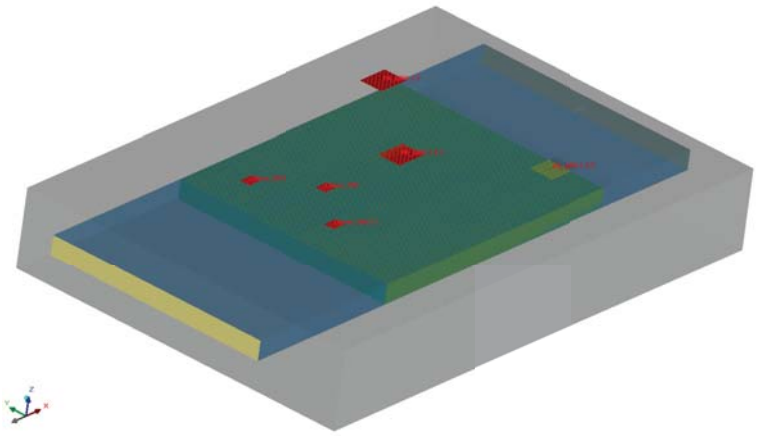

Figure 2.21: Simple simulation model

The hardware used for the numerical simulations consists of Intel i7 8700 processor (6 cores), Nvidia GTX1070 graphic card unit (GPU) and 24 GB 2400 MHz ram. PC operating system is Microsoft Windows 10 which has two percent CPU usage and ten percent ram usage at idle state.

The result of simulation run speed investigation is presented in Table 2.4. The mesh network is regenerated for each run and included in the duration. The HyperThread (HT) technology is developed by Intel which creates an additional virtual core for each physical core of the processor. This technology is open to arguments for numerical simulation capabilities, therefore it's effect is also evaluated. The fastest simulation run achieved by solution settings of 6 parallel cores, GPU enabled and HyperThread enabled. Although the effect of GPU is rather insignificant in this case, the GPU can decrease run duration dramatically when solving for radiation heat transfer, for example for a satellite thermal analysis. The effect of Intel's HyperThread technology is also found ineffective for Icepak CFD analysis. The results lead to the conclusion that for CFD simulations, the number of the physical cores of the

processor is the most important hardware specification. Even though all simulation parameters are identical, the resulting maximum temperature (observed under center PA chip with 60 W heat dissipation) in the model differs up to 0.07°C between runs. A possible explanation for this phenomena is that each run stops at slightly different convergence rate.

Table 2.4: Results of simulation run speed investigation

Run	**HT**	**Parallel Cores**	**GPU**	**Duration (seconds)**	**Maximum Temperature (°C)**	**Pressure Drop (bar)**
1	on	12	Enabled	672	64.48	0.70
2	on	12	-	773	64.48	0.70
3	on	6	-	671	64.55	0.70
4	on	3	-	813	64.51	0.70
5	on	6	Enabled	655	64.55	0.70
6	off	6	Enabled	676	64.55	0.70

2.3.2 CFD Model of Numerical Simulations

Based on module CAD designs, modules are remodeled in ANSYS-Icepak environment by using software specific modeling features since importing CAD geometry directly results in poor meshing capabilities. The hex-dominant Mesher-HD algorithm is used for mesh network creation. The simulation model is constructed using blocks, sources, openings, and sources. Natural convection is assumed insignificant and all outer surfaces are modeled as adiabatic walls. The inlet and outlet interfaces of the modules are simplified by prismatic form with identical cross-section area rather than complex cylinder shape with threads and liquid connector details. The materials of solids and liquids are modeled accordingly wherein aluminum modules, two module parts are modeled with different aluminum alloys of Al 1100 and Al 6061.

The inlet boundary conditions are determined according to the liquid passage height of each module in order to obtain 2 lpm flow rate. Inlet liquid temperature is set to 25 °C. Outlet boundary condition is given as static atmosphere pressure at sea level.

Heat sources modeled according to dimensions and heat dissipations of the diamond resistors. They are modeled as two-dimensional sources since the focus is on the temperature distribution on the module rather than diamond resistor junction temperatures.

The microchannels modeled according to channel height and fin density of each module. The solid fins in microchannel heat sink are modeled as a solid block rather than built-in "Heat Sinks" feature of Icepak in order to establish a better control on their mesh. The simulation model is presented in Figure 2.22.

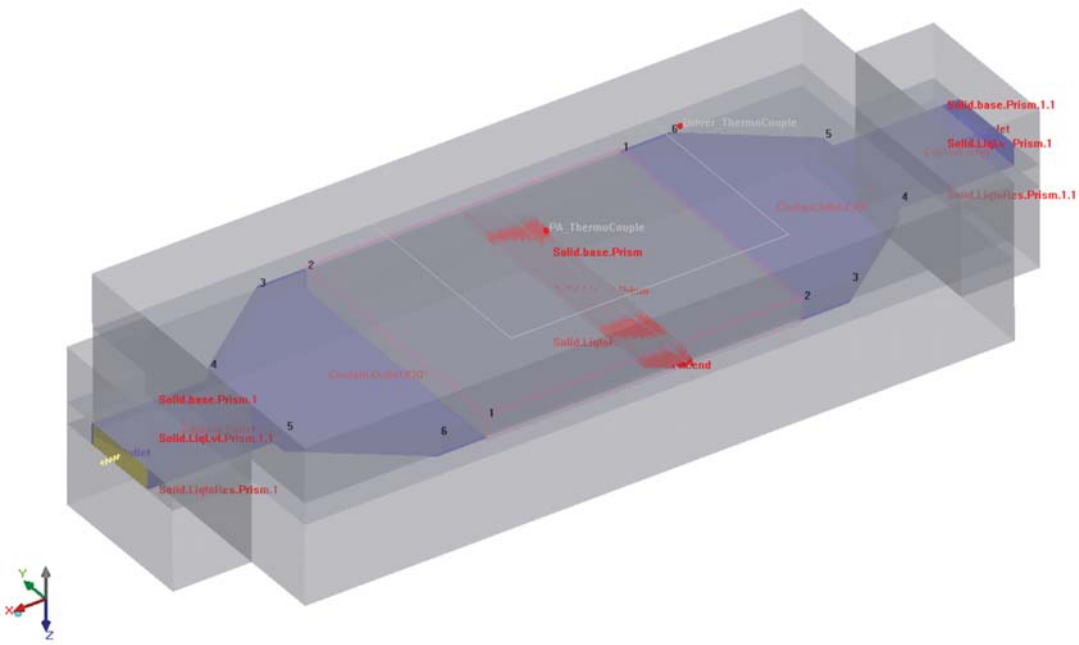

Figure 2.22: The simulation model for alternative module analyses

Icepak uses ANSYS-Fluent which solves conservation equations for mass and momentum based on Navier-Stokes equations. The user guides of ANSYS-Icepak and ANSYS-Fluent explain the solution methodology in details. The general form of conservation of mass equation (or continuity equation) used in Fluent is given in Equation 2.2.

$$\frac{\partial \rho}{\partial t} + \bigtriangledown \cdot (\rho \vec{v}) = S_m \tag{2.2}$$

where ρ is the fluid density, $\vec{v}$ is the velocity vector and S_m is the mass added to

the continuous phase from the dispersed second phase and from other user-defined sources.

The general form of conservation of momentum equation solved by ANSYS-Fluent is given in the Equation 2.3.

$$\frac{\partial(\rho\overrightarrow{v})}{\partial t} + \nabla \cdot (\rho\overrightarrow{v}\,\overrightarrow{v}) = -\nabla p + \nabla \cdot \overline{\overline{\tau}} + \rho\overrightarrow{g} + \overrightarrow{F} \tag{2.3}$$

where ρ is the fluid density, $\vec{v}$ is the velocity vector, p is the static pressure, $\overline{\overline{\tau}}$ is the stress tensor, $\rho\overrightarrow{g}$ is the gravitational body force, and $\overrightarrow{F}$ is the external body forces including other model-dependent source terms such as porous-media and user-defined sources.

The stress tensor $\overline{\overline{\tau}}$ is defined as follows.

$$\overline{\overline{\tau}} = \mu[(\nabla\overrightarrow{v} + \nabla\overrightarrow{v}^T) - \frac{2}{3}\nabla \cdot \overrightarrow{v}I] \tag{2.4}$$

where μ is the molecular viscosity, I is the unit tensor and $\nabla\overrightarrow{v}^T$ is the effect of volume dilation.

Smooth, regular, deterministic, and steady characteristics of laminar flow allow ANSYS-Icepak to establish a solution by solving classical Navier-Stokes and energy conservation equations. On the other hand, turbulent flow can be considered random, chaotic, non-deterministic, and essentially unsteady due to the statistical fluctuations. Therefore, the classical Navier-Stokes and energy conservation equations are not sufficient for an accurate solution in turbulent flows.

ANSYS-Icepak solves the Reynolds-averaged forms of these equations so that the stochastic fluctuations are smoothened out. There are eight solution algorithms available in ANSYS-Icepak for turbulent flows classified as zero-equation turbulence model and advanced turbulence models. According to the flow characteristics of the numerical model of this study, turbulent flow models of zero equation, enhanced two equation and Spalart-Allmaras are selected for further investigation.

The zero equation turbulence model (also known as the algebraic model) calculates

the turbulent viscosity μ_t using the mixing-length with the following relation.

$$\mu_t = \rho(l^2)S \tag{2.5}$$

where ρ is the fluid density, l is the mixing-length, S is the modulus of the mean rate-of-strain tensor. The mixing-length l defined as follows:

$$l = min(kd, 0.09d_{max}) \tag{2.6}$$

where d is the distance from the wall and the von Kármán constant k = 0.419.

The mean strain rate S is defined as follows:

$$S = \sqrt{2S_{ij}S_{ij}} \tag{2.7}$$

where the mean strain rate S_{ij} is calculated by the following equation.

$$S_{ij} = \frac{1}{2}(\frac{\partial u_j}{\partial x_i} + \frac{\partial u_i}{\partial x_j}) \tag{2.8}$$

The enhanced two-equation model is basically an advanced turbulence model which combines three two equation (K-ε) models (standard, RNG and realizable) with enhanced wall treatment in order to more accurately resolve the flow near the wall. These two equation models (standard, RNG and realizable) are developed mainly for the turbulent core flows (in the regions somewhat far from walls). Therefore, to make these models suitable for wall-bounded flows, additional measures are to be considered. The presence of walls have a significant effect on turbulent flows considering the mean velocity field is affected by the no-slip condition at the walls. In addition, the turbulence is also affected by the presence of the wall in non-trivial ways such as the viscous damping reduces the tangential velocity fluctuations close to the wall and kinematic blocking degrades the normal fluctuations. The near-wall modeling can tremendously improve the accuracy of numerical simulations of turbulent flows, inasmuch as walls are the main source of mean vorticity and turbulence. At the near-wall region, the momentum and other scalar transports are the greatest and the solution variables have large gradients. Therefore, an accurate flow representation at the near-wall region is required in order to achieve successful predictions of wall-bounded

turbulent flows [31, 32]. Originally, the Spalart-Allmaras model is a low-Reynolds-number model which requires the viscous-affected region of the boundary layer to be resolved in high quality [33]. However, ANSYS Icepak implemented the Spalart-Allmaras model in order to use wall functions even though the mesh resolution is not sufficiently fine.

2.3.3 Investigation of Mesh Independence and Flow Regime

The mesh network of a numerical simulation model is imperative to obtain results with high accuracy. The mesh network created by Icepak Mesher-HD algorithm according to meshing parameters. For an optimum mesh network, the simulation model is split into assemblies with specific mesh parameters. The mesh network for liquid passage, especially in microchannels requires much smaller elements in order to achieve a close resemblance of the boundary characteristics. In addition, split assemblies aid avoiding mesh bleeding.

Therefore, a mesh independence study conducted to establish an optimum mesh network with necessary accuracy while aiming a minimum number of elements for shorter calculation durations. The simulation outputs selected for the investigation as the maximum temperature on the top surface of the module, maximum liquid flow speed and pressure drop (DP) between the inlet and outlet of the module. The study conducted on the simulation model of copper microwave module with 85 FPI fin density, considering mesh is more critical in the smallest channel case. The mesh independence study is presented in Table 2.5. The mesh network with 2.63 million elements is selected as the best mesh network.

Table 2.5: Results of mesh independence investigation

No. of Elements	**Max. Temperature(°C)**	**Max. Flow Speed (m/s)**	**DP (bar)**
411768	151.00	0.459	0.1772
1285329	152.44	0.606	0.1820
2632114	127.14	0.608	0.1827
3424630	127.13	0.608	0.1828
5422687	127.09	0.608	0.1830

The details of the mesh structure of selected mesh network with 2.63 million elements are presented in Figure2.23 where the mesh network at the midsection of the module is presented at three different level by zooming towards the microchannels. There are minor mesh bleedings present in the mesh network which is introduced by the Mesher-HD algorithm. These mesh bleedings cannot be omitted without sacrificing the mesh resolution and they were not a concern for solution accuracy but they cause an ignorable increase in the solution run time.

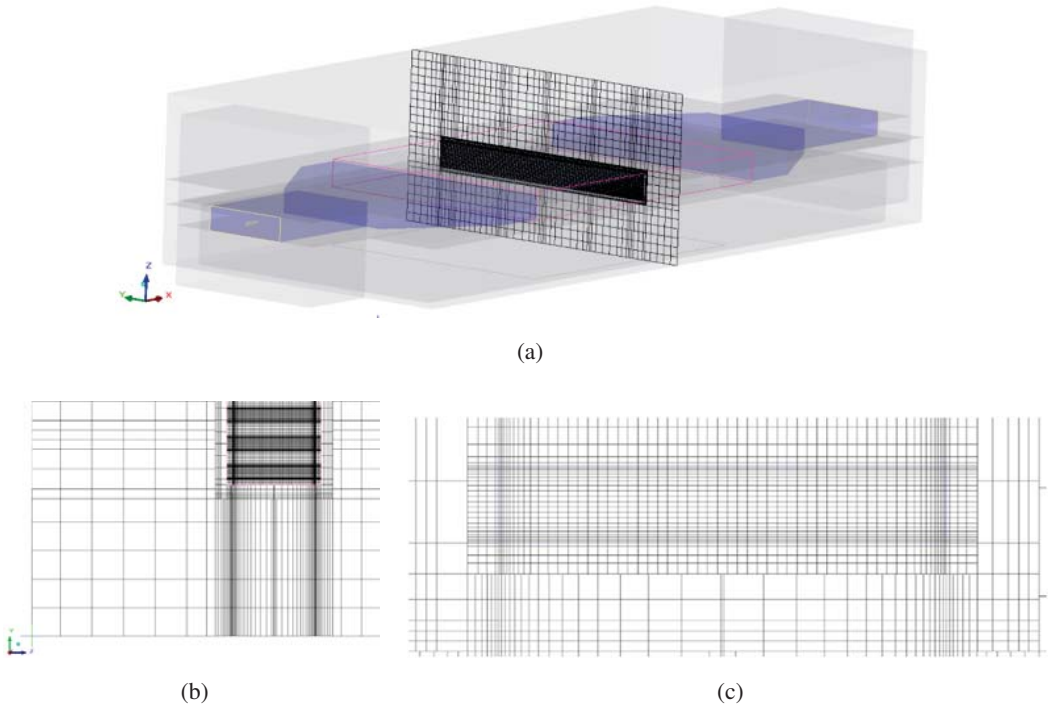

Figure 2.23: Details of selected mesh network at module mid section (a) Overall module view (b) Zoomed view of three microchannels (c) Zoomed view of one microchannel

The flow regime is also of great importance for a successful CFD analysis. In this study, the flow is a single-phase liquid with forced convection. Reynolds number (Re) is the key parameter to analyze flow characteristics. By comparing viscous effect to the inertia effect, the dimensionless Reynolds number identifies the flow regime as laminar (Re < 2300), transition (2300 < Re < 4000) and turbulent (Re > 4000).

For rectangular ducts, hydraulic diameter is used in Reynolds Number calculations, as shown in Equations 2.9 and 2.10.

$$Re = \frac{uD_h}{v} \tag{2.9}$$

where u (m/s) is velocity based on the actual cross section area of the duct, v (m^2/s) is kinematic veloctiy and D_h (m) is hydraulic diameter.

$$D_h = \frac{4A}{P} \tag{2.10}$$

where A (m^2) is section area of the duct and P (m) is the wetted perimeter of the duct.

The flow passage in the module is divided into sections according to the flow speed and the hydraulic diameter, as shown in Figure 2.24. The flow speed data is taken from simulation results (at 2 lpm flow rate) and maximum speed value taken for each section. Reynolds numbers are calculated for the liquid flow in module alternatives and presented in Table 2.6 where kinematic viscosity of Glycol50 is 4.251×10^{-6} m^2/s. The results conclude that the flow is laminar in microchannels and turbulent in the expansion/contraction sections and inlet/outlet sections. The turbulent behavior is relatively more present in modules with shorter height and higher fin density, specifically in module 2.

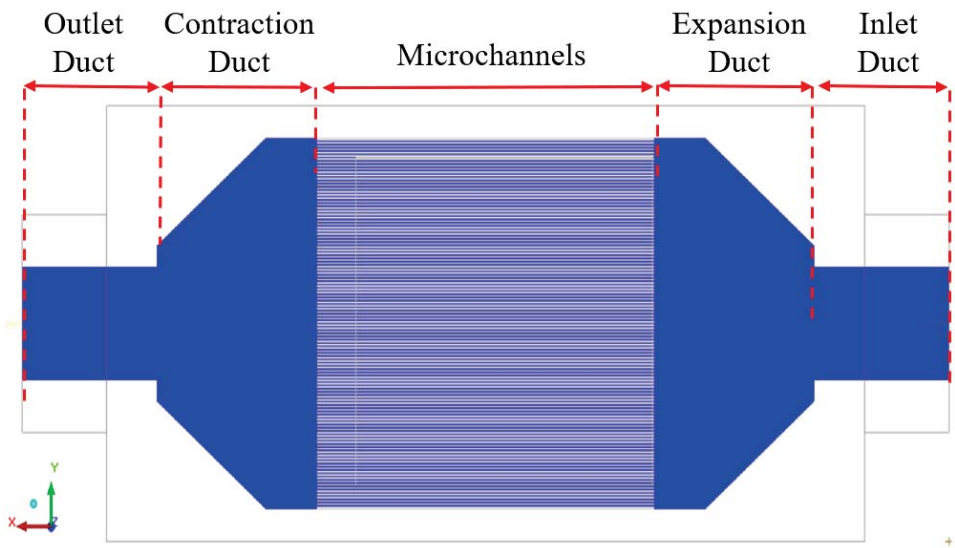

Figure 2.24: Sections of liquid flow in modules

Table 2.6: Reynolds numbers of alternative modules at different sections of flow passage

Module	**Duct Width (mm)**	**Duct Height (mm)**	**Dh**	**Re**
Microchannels				
1	0.5	1.78	0.0017	646
2	0.15	2.9	0.0006	191
3	0.5	5	0.0018	265
4	0.15	2.75	0.0006	108
Inlet and Outlet Duct				
1	10.4	1.78	0.0091	3072
2	10.4	2.9	0.0061	3389
3	10.4	5	0.0135	2923
4	10.4	2.75	0.0087	3131
Expansion and Contraction Duct				
1	30.15	1.78	0.0106	3584
2	30.15	2.9	0.0067	3748
3	34.15	5	0.0174	3775
4	34.15	2.75	0.0102	3664

ANSYS Icepak also calculates the Reynolds number prior to each run with the aim of warning the user about the flow regime selection. The investigation on flow equations is conducted by using the simulation model of module 4 (copper with 85 FPI fin density). Icepak suggests flow is laminar by calculating Reynolds number up to 753.89 (highest values presented for Module 2). Even though the simulation software and Reynolds number analysis strongly suggest the flow is in laminar region, simulation runs conducted with the selected mesh network for different flow regime equations as shown in Table 2.7. The minimal difference between laminar and turbulent equations supports the software's claim of laminar flow in the module.

Table 2.7: Results obtained from different flow regime equations

Flow Eq.	Max.Temperature (°C)	Max.Flow Speed (m/s)	DP (bar)
Laminar	69	1.76	0.612
Spalart-Allmaras	68.9	1.76	0.615
Zero Equation	68.8	1.65	0.633
Enhanced two equation	68.9	1.77	0.617

2.3.4 Results and Discussion of Numerical Simulations

The Icepak CFD model is created by using parametric model features. Therefore, the simulation runs can be performed for each module alternative by changing model parameters of module material and liquid passage dimensions. Prior to simulation runs post-processing monitoring points are created at determined thermocouple locations in order to have a comparison between simulations and experiments, as shown in Figure 2.25.

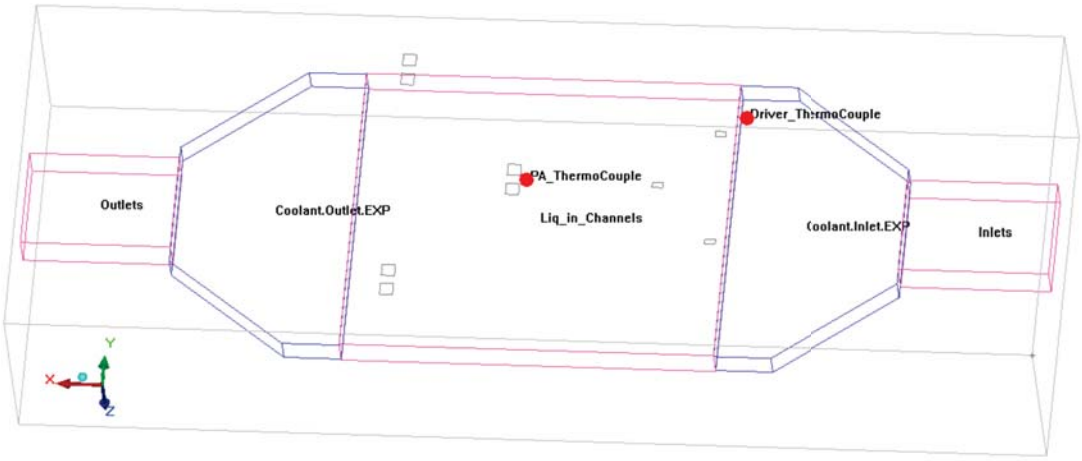

Figure 2.25: The simulation model for alternative module analyses

The results are presented by using the module descriptions given in Table 2.2 as module 1 (Aluminum with 25 FPI fin density), module 2 (Aluminum with 85 FPI fin density), module 3 (Copper with 25 FPI fin density) and module 4 (Copper with 85 FPI fin density). As a rule of thumb, there is a trade-off between temperature values and pressure drop in proper cold plates. Even though, the main objective of this study is to keep module temperatures minimum, the pressure drop along the modules' liquid passage is to be carefully analyzed to determine necessary pump power. Firstly,

temperature distributions of the module top surfaces are presented in Figure 2.26.

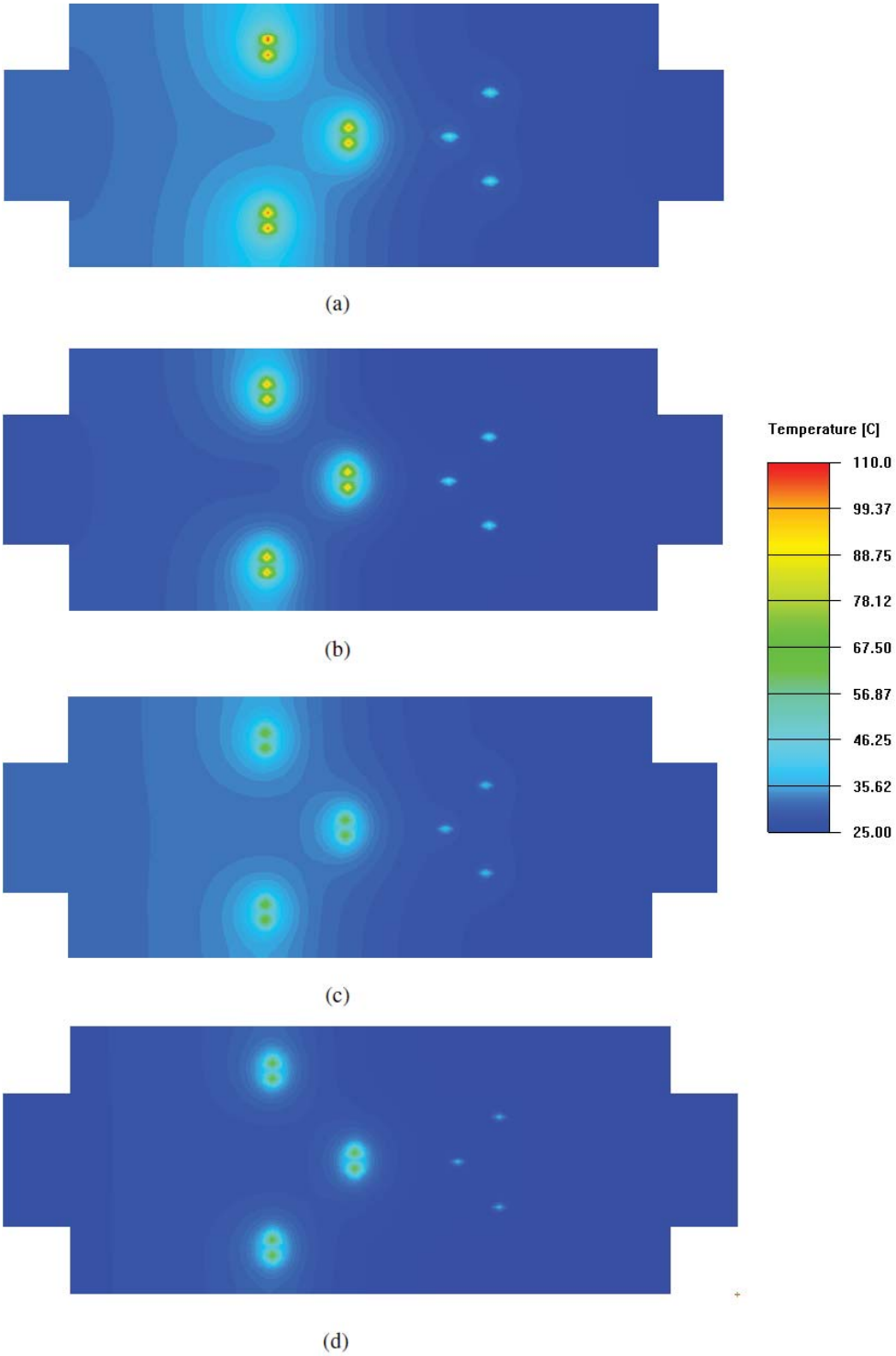

Figure 2.26: Temperature distributions of the module top surfaces (a) Module 1 (b) Module 2 (c) Module 3 (d) Module 4

The velocity distributions at mid liquid passage x-cut of the modules are presented

in Figure 2.27, where the flow characteristics in microchannels can be observed. The pressure distribution at mid liquid passage z-cut of module 4 (module with highest pressure drop) is presented in Figure 2.28. The velocity distribution at mid liquid passage z-cut of the modules are presented in Figure 2.29.

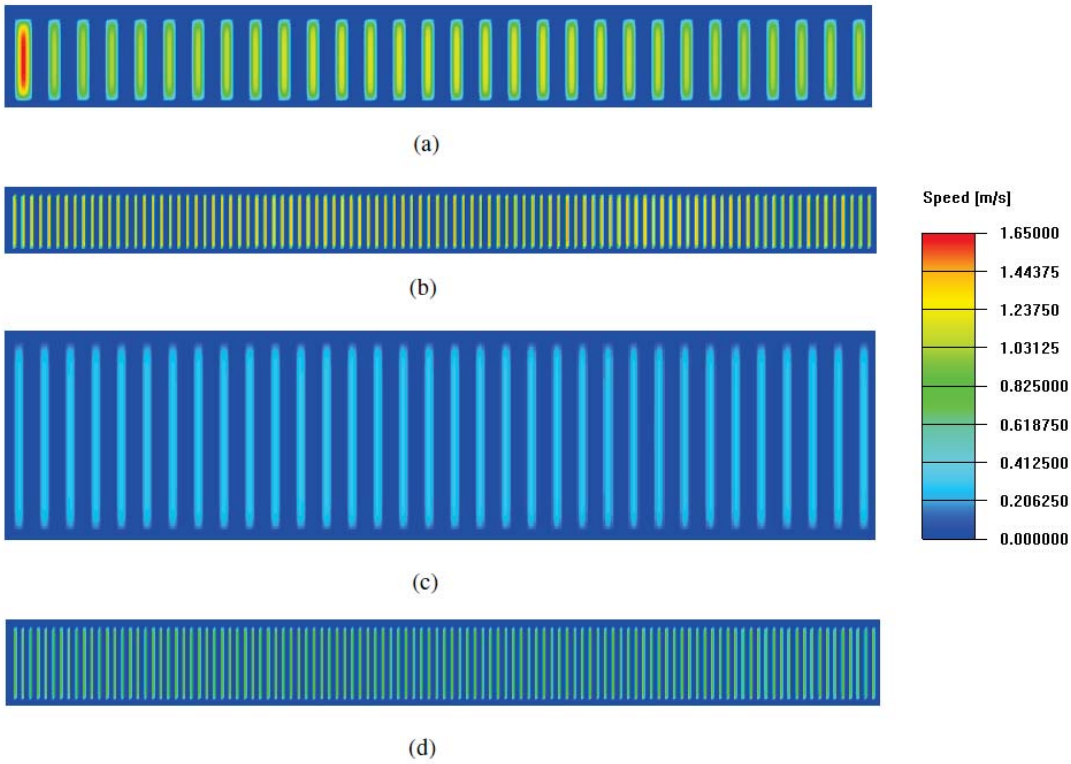

Figure 2.27: Velocity distribution at mid x-plane of liquid passage of the modules (a) Module 1 (b) Module 2 (c) Module 3 (d) Module 4

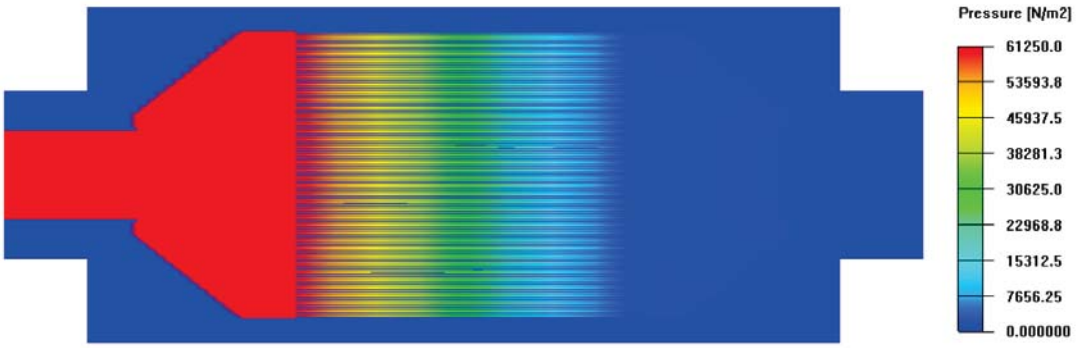

Figure 2.28: Pressure distribution at mid z-plane of liquid passage of module 4

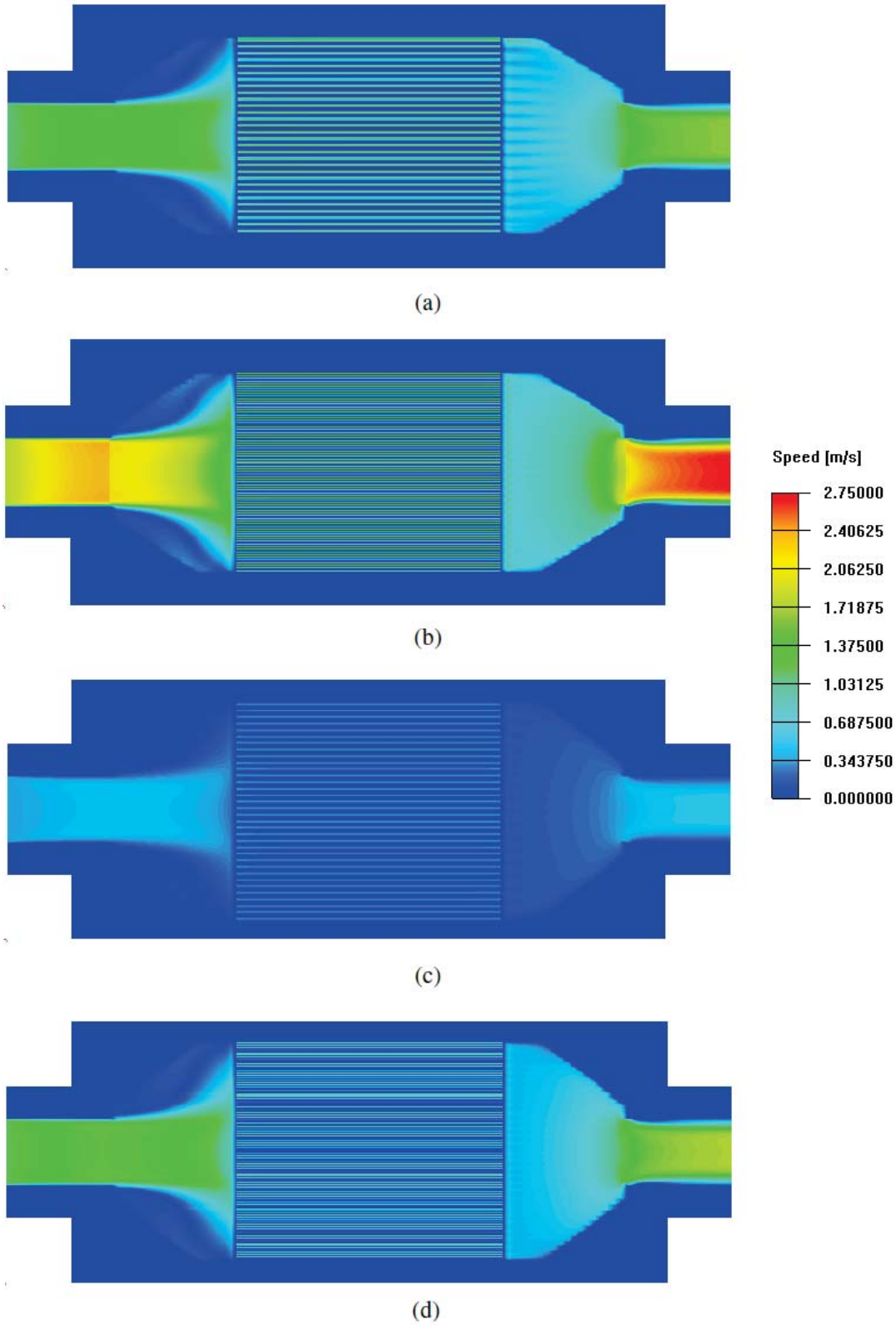

Figure 2.29: Velocity distribution at mid z-plane of liquid passage of the modules (a) Module 1 (b) Module 2 (c) Module 3 (d) Module 4

The summary of the numerical simulation results is presented in Table 2.8. The results are clearly highlighting the performance gain through an increase in fin density and increase in material thermal conductivity.

Table 2.8: Numerical Simulation Results

	Module 1	**Module 2**	**Module 3**	**Module 4**
Max. Temperature (°C)	107.6	102.4	72.35	69
TC PA mid (°C)	50.905	47.145	41.814	37.972
TC PA side (°C)	42.892	38.383	37.535	33.001
TC Driver (°C)	28.581	26.81	28.436	26.161
Max. Flow Speed (m/s)	1.663	2.719	0.945	1.76
DP (bar)	0.088	1.097	0.041	0.61

As seen in Figure 2.27, velocity distribution among microchannels can be considered uniform with the exception of first and last channels where the channel dimensions are different due to manufacturing concerns. The difference in velocity profiles of microchannels is clearly seen in Module 1 where the first microchannel has the highest liquid flow rate due to a dimensional difference.

In aluminum modules, the fin density increase from 25 FPI to 85 FPI resulted with 5.2 °C (4.8%) decrease in maximum temperature, 3.76 °C (7.4%) decrease in TC PA mid temperature and 1.01 bar (12.5 times) increase in pressure drop.

In copper modules, the fin density increase from 25 FPI to 85 FPI resulted with 3.35 °C (4.7%) decrease in maximum temperature, 3.84 °C (9.2%) decrease in TC PA mid temperature and 0.57 bar (14.9 times) increase in pressure drop. The height of liquid passage and microchannel fins are longer in copper modules compared to the aluminum modules. Therefore, pressure drops are significantly lower in copper modules compared to aluminum ones. The height difference between modules is the result of the limitations of the aforementioned microchannel manufacturing technique.

At 25 FPI fin density, the simulation results of copper module show that the maximum temperatures are 35.25 °C (32.8%) and PA mid thermocouple temperatures are 9.1 °C (17.9%) lower than an aluminum module. In addition, the pressure drop is 0.047 bar (about half) lower in copper module compared to aluminum one.

At 85 FPI fin density, the simulation results of copper module show that the maximum temperatures are 33.4 °C (32.6%) and PA mid thermocouple temperatures are 9.2 °C (19.5%) lower than an aluminum module. In addition, the pressure drop is 0.047 bar (about half) lower in copper module compared to aluminum one.

The simulation results suggest the copper module with 25 FPI fin density (Module 3) is promising the optimal balance between cooling performance and pressure drop. The results also show that the cooling performance increase by increased fin density is very limited compared to material change with higher thermal conductivity. Due to the aforementioned relation between the RF PA chip mean lifetime and its junction temperature; the limited temperature decreases are considered significant for the design covered in this study.

CHAPTER 3

EXPERIMENTAL PROCEDURES AND RESULTS

This chapter is divided into three main sections. In Section 3.1, the experimental setup is explained with details of participating devices and equipment. In Section 3.2, the experimental procedures and measures taken during experiments are presented. In the last part of this chapter, the experimental results are presented with a discussion. In the discussion, the experimental results compared with the numerical simulation results of Chapter 2.

3.1 Experimental Setup

3.1.1 Manufacturing Microwave Modules with Microchannels

The microwave modules produced according to the CAD drawings presented in Section 2.2.1. According to their materials of copper and aluminum, slightly different manufacturing methods used for module production as explained in detail in the mentioned section. The modules manufactured in two separate facilities of the manufacturer company located in China and USA. After all manufacturing and post-manufacturing processes are completed, the modules delivered to ASELSAN. The photos of four alternative microwave modules presented in Figure 3.1.

The diamond resistors are mounted on microwave modules at predetermined locations in a cleanroom environment according to process rules of microwave electronics manufacturing. In addition, the power supply cable harness and necessary connections between diamond resistor pins and power lines are produced. The module with

diamond resistors and cabling is shown in Figure3.2.

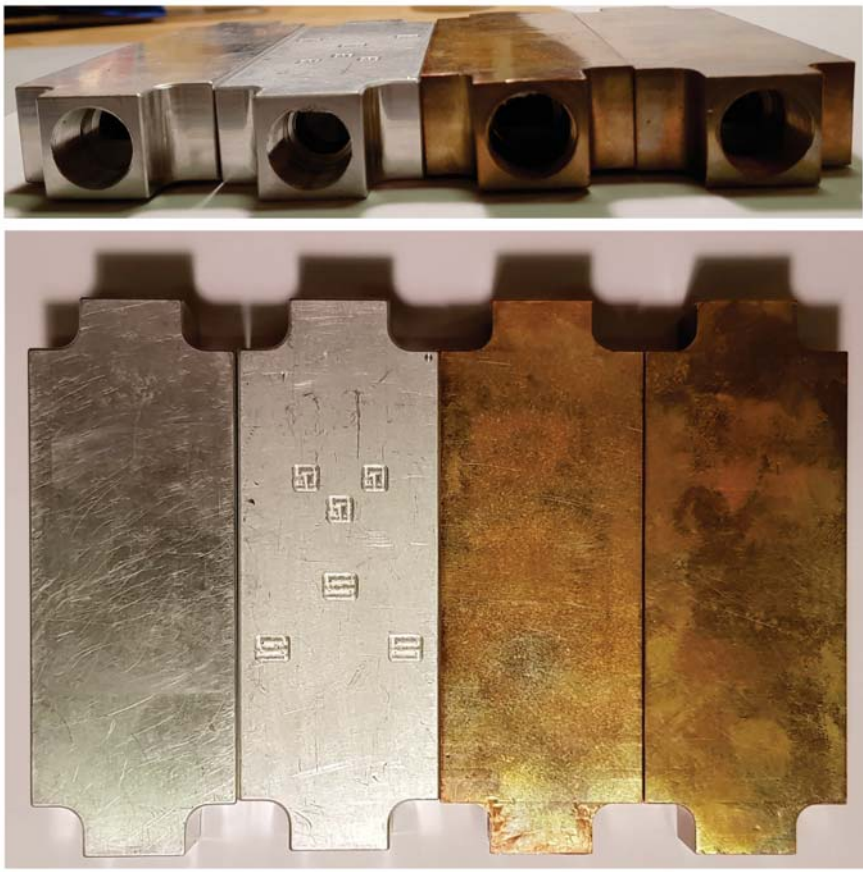

Figure 3.1: Manufactured microwave modules layout

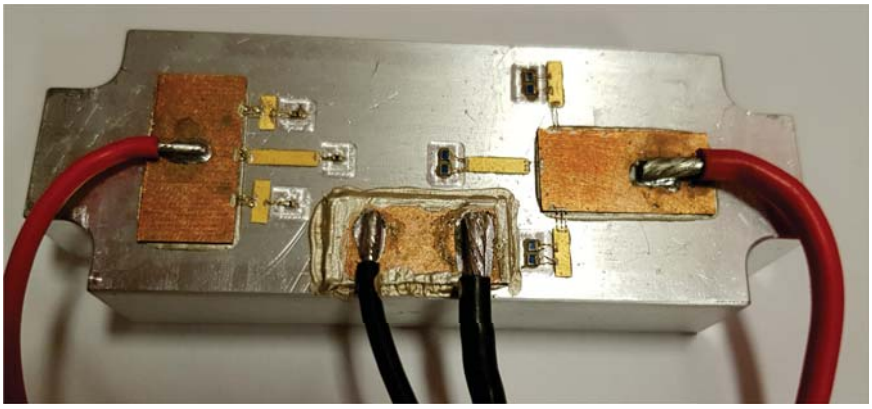

Figure 3.2: The module with diamond resistors and cabling

For temperature readings, J-type thermocouples (from Omega) are placed on predetermined locations on the top surface of the module. Although it is preferable to retrieve the temperature readings from underneath the heat dissipating diamond resistors, it is practically impossible without manipulations on the module. Therefore,

thermocouples are placed on convenient positions closest to the diamond resistors. It is intuitive and also seen from numerical simulations that the highest temperature values are seen around the 50W diamond resistors (two of them closely placed, dissipating 60 Watts in total), while among them the highest temperature is experienced at center placed one. Thermocouples supplied as lengthy cable wound around a drum to be cut for the desired length. Thermocouples are cut in 1.5m length and before placing them on the modules, their open ends are welded using Omega TL-WELD arc weld device. The thermocouples are placed accordingly as shown in Figure3.3.

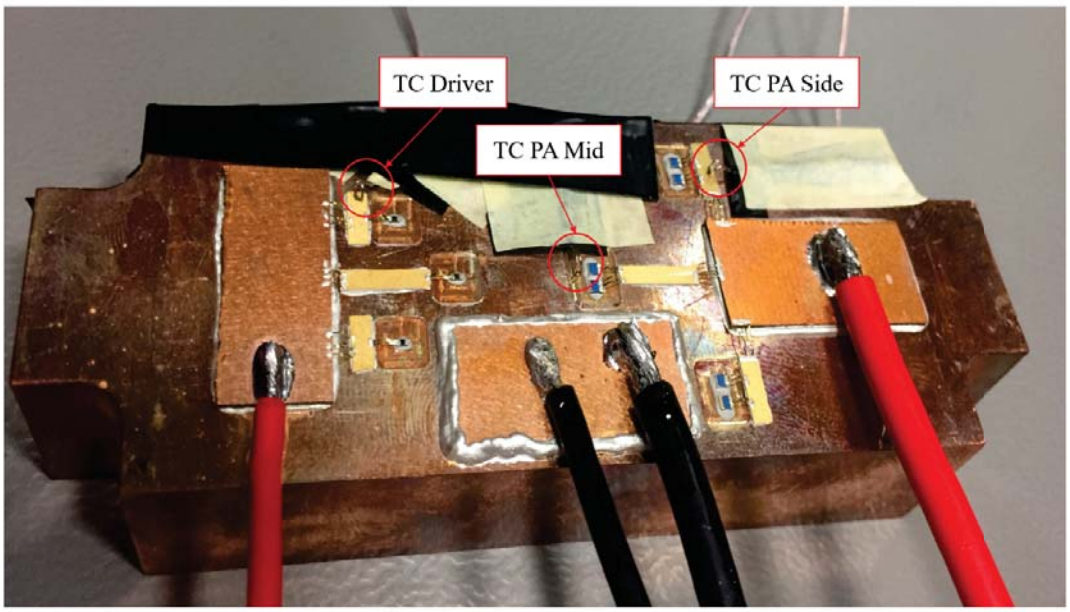

Figure 3.3: The thermocouple measurement locations on modules

The modules have inlet/outlet threaded interfaces compatible with the selected CGD-05 type liquid connectors from Stäubli. These connectors are the manifold type, meaning that they need a physical force to be held in place. Due to this limitation and the already present necessity for an adaptor part for pressure transmitters measurements, these quick connects are not used in experiments. Instead, the adaptor part of pressure transmitters is designed accordingly to fit the inlet/outlet threaded interfaces of the modules. After these procedures applied, the microwave modules with microchannels are ready to become the test specimens of the experiments.

3.1.2 Custom Liquid Control Unit and Manufacturing Pressure Transmitter Adapter

For experiments, a liquid control unit is necessary to supply liquid to modules with desired specifications. Due to limited accuracies and capabilities of available liquid control units at ASELSAN, it is decided that a custom liquid control unit with advanced control and measurement features is necessary. The custom liquid control is defined to an experienced local subcontractor firm selected among several candidates. The unit is designed and manufactured by ISISO Mekatronik Mühendislik Savuma Sanayi ve İklimlendirme Sistemleri A.Ş. The specifications of the liquid supply unit and unit photo are presented in Figure3.4. It should be noted that this study carried parallel to an ASELSAN research and development project with a strict schedule. Even though author's intention is to work with a compact liquid supply unit with higher accuracies in supplied liquid temperature and flow rate; the company decision was towards acquiring a liquid supply unit with a much bigger pump in order to use it in future overall unit (the unit consists of several microwave modules with microchannels) level tests. The ISISO liquid supply unit still had all features intended by the author but with lessened precision in mentioned metrics. These intended features are electronically controlled valves for flow rate setting (a bypass pipeline included in unit to help increase the accuracy of flow rate of delivered liquid), a refrigeration cycle, a heating resistor in liquid reservoir (to be able to conduct tests above room temperature), pressure transmitters at exit and return liquid lines, temperature measurements (thermocouples placed at liquid reservoir, exit and return liquid lines) and a software with touchscreen interface to control all these parameters and to read measurements. The touchscreen enables the user to set the liquid flow rate and liquid temperature and read the measurements of temperature and pressure drop.

The liquid supply unit specifications are in Turkish in Figure3.4 due to local production. The main specifications of the unit are as follows.

- Package liquid conditioning unit with 2.5 kW cooling capacity
- -5 °C evaporation and +45°C condensation capacity
- Supplied liquid temperature range of -5 °C to +45°C

- Internal components of 35 m2 condenser, EBM 45-5K fan motor, MIT 5/36 plate type evaporator, ETNA M-46-T/1.5 kW pump
- PLC automation control with touch screen interface, as shown in Figure3.5

Figure 3.4: The custom liquid control unit

Figure 3.5: User Interface of the custom liquid control unit

The control interface, shown in Figure3.5 the has liquid temperature and flow rate settings on the left side. On the right side, the measurements of actual liquid flow rate, the pressure drop between exit and return and temperatures of liquid at exit and return are present. The measurements provided by the liquid control unit are less

than ideal due to their locations and precision. The hoses between the unit and test specimen present additional pressure drop and introduce additional heat dissipation to the environment even if insulated carefully. Therefore, additional measurement equipment used in experiments.

Pressure measurements should be taken at the closest accessible location to the inlet and outlet of the modules for accurate pressure drop calculation. For this reason, a mechanical adaptor part is designed to integrate pressure transmitters even though the pressure drop readings are available at the liquid control unit. The pressure transmitter adaptor is designed and manufactured in a minimalistic fashion to achieve three open interfaces for liquid inlet, pressure transmitter and a liquid outlet. The openings of the adaptor part are connected respectively with the module, pressure transmitter from WIKA and SPH-08 liquid connectors from Stäubli (to mate with a liquid connector of either flow meter or liquid supply hose.The adaptor is manufactured from an aluminum cylinder where a hole drilled across its central axis, another hole drilled on the side (asymmetrically located, i.e. positioned closer to test specimen) for pressure transmitter mounting and threads tapped on all three openings compliant to their mates, as shown in Figure3.6. mates, as shown in Figure3.6.

Figure 3.6: The pressure transmitter adaptors

3.1.3 Equipment and Devices Used in Experiments

The experimental setup is formed by the liquid supply unit (including hoses, couplings and liquid reservoir of Glycol50), a data acquisition, a laptop with data acquisition software, a multiplexer, a flow meter, thermocouples, pressure transmitters

adaptor, pressure transmitters, liquid connectors, insulations, power supplies, cables, and multimeters. The list of equipment and devices used in experiments are presented in Table 3.1. Two separate power supplies are required due to the presence of two different type of diamond resistors with heat dissipation rates of 5 W and 30 W.

Table 3.1: Numerical Simulation Results

Purpose of Use	**Description**	**Quantity**
Liquid Control Unit	ISISO 151221/1	1
Data Acquisition Unit	Agilent 34970A	1
20 Channel Multiplexer	Agilent 34903A 20-Channels	1
Laptop	HP Compaq nc8430	1
Software	BenchLink Data Logger 3	-
Flow Meter	Siemens MASSFLO 6000	1
Thermocouples	OMEGA J type	several
Pressure Transmitter	WIKA Type A-10	2
Liquid Connectors	Stäubli SPH-08	4
Multimeter	FLUKE 87	1
Multimeter	FLUKE 117	1
Power Supply	Hewlett Packard E3615A	1
Power Supply	Keysight 6032A	1

3.2 Experimental Procedure

The experiments conducted at ASELSAN Thermal Design Laboratory, a densely packed temperature-controlled room with about 120 m^3 volume. The room temperature kept at 25 °C by air-conditioner during experiments. Prior to experiments, the diamond resistor connected to two separate power supplies to check the health of their wiring, bonds, and connections. According to power supply readings, the diamond resistors dissipates the determined amount of heat. These measurements are done in very short duration (below 1 second) to avoid any damage to diamond resistors and electrical connections. Afterward, the modules and power supplies carried to the Aselsan Thermal Design Laboratory where all remaining components of the experi-

ment setup are readied. First, the test specimen module is connected to the pressure drop adapters where pressure transmitters installed. The assembly of the module and pressure transmitters are connected to the flow meter as shown in Figure 3.7.

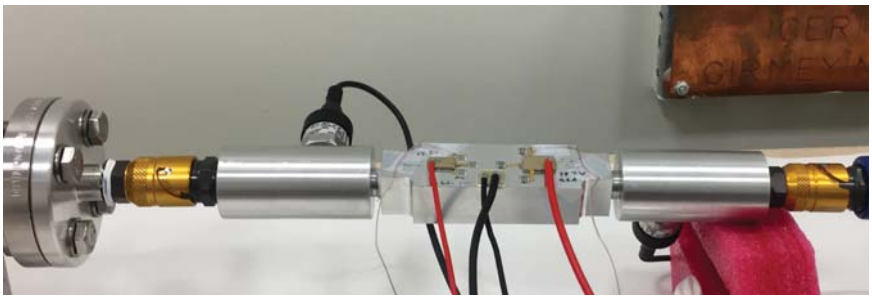

Figure 3.7: The assembly of the module and pressure transmitters

The power supply cables connected to power supplies according to diamond resistor heat dissipations. The hoses of the liquid control unit are connected to pressure transmitter adaptor at the module inlet side and the flow meter. The experimental setup before applying the insulation is shown in Figure 3.8.

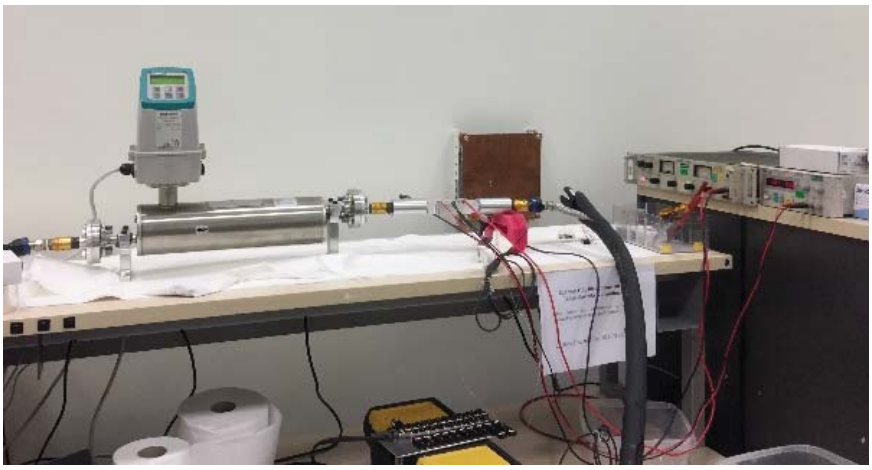

Figure 3.8: Experimental setup with power supplies before insulation application

Measures were taken to block the heat loss to the environment through natural convection by applying several layers of insulations. For insulation, foam hose insulation material with the lowest available thermal conductivity is selected. The insulation application is presented in Figure 3.9. The pressure transmitters require electrical power at 5V, therefore an additional power supply is used to power them. Initially, the data cables of pressure transmitters are connected to two multimeters for pre-experiment controls.

Figure 3.9: Insulation of module and pressure transmitter adaptors

Later, the wires of thermocouples and pressure transmitters are connected to the multiplexer card of the data acquisition device. For ease of application, an interface board is built with socket connectors in order to serve as an interface between multiplexer card (which is installed inside the data acquisition device) and connectors of thermocouples and pressure transmitters. The interface board and data acquisition device is presented in Figure 3.10. The data acquisition device is connected to the laptop with the data logger software where measurement is read in real time as shown in Figure 3.11.

Figure 3.10: Photos of interface board (left) and data acquisition device (right)

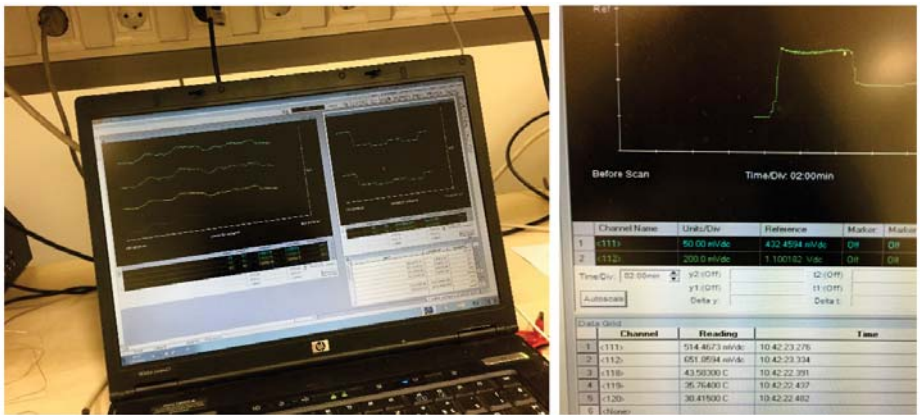

Figure 3.11: Real time experimental measurement through data logger software

To conclude, all necessary connections of power cables, data cables, and liquid hose are completed and experimental setup is prepared for control run. The liquid control unit is turned on and set for supplying liquid at 25°C with a flow rate of 2 lpm. The flow meter is used to double check the flow rate as shown in Figure 3.12.

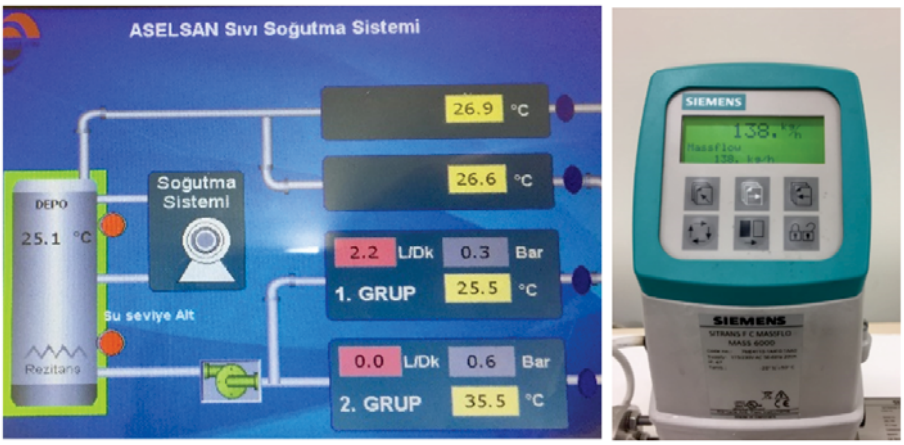

Figure 3.12: Liquid control unit interface (left) and flow meter (right)

According to flow rate readings, the power supplies of diamond resistors are enabled for initial temperature measurements as shown in Figure 3.13. The readings from the power supply states that the three diamond resistors with 5 W heat dissipation are dissipating 5.06 W. The aforementioned diamond resistors simulating the main PA chip (60 W) are placed in groups of two where each dissipates 30 W. The power supply data saturates at 39 V with 4.7 A which powers all six diamond resistors. Therefore each diamond resistor dissipates 30.55 W individually and 61.1 W in a combination of two.

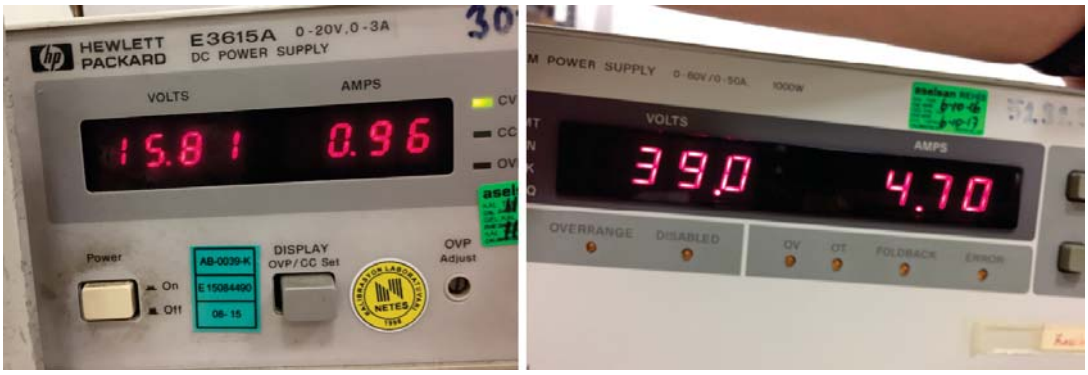

Figure 3.13: Power supply settings of the diamond resistors with 5 W heat dissipation (left) and 30 W heat dissipation (right)

Due to insulations, usage of a thermal camera is impossible. In order to get a visual understanding of temperature distribution, a thermal camera is brought to the experimental setup. The thermal camera image of the uninsulated module 1 (in which the highest temperatures are expected) is presented in Figure 3.14 where flow rate decreased to 1 lpm. The thermal camera image shows that the aforementioned design objective of keeping the diamond resistor temperatures under 125°C is satisfied by a safety margin. The high-temperature resistant bands which are holding the thermocouples in place were reflective and gave a wrong temperature reading in areas surrounding them.

Figure 3.14: Thermal camera image (left) and thermal camera setup (right)

In summary, the microwave modules are connected to the liquid control unit, data acquisition system, and power supplies where determined heat dissipations are provided by diamond resistors while liquid supplied at 25°C with a flow rate of 2 lpm. The measurements of pressures and temperatures are digitally collected for the experiment.

3.3 Experimental Results

Due to the limited precision of the liquid control unit at low flow rates, the unit reached steady state conditions at slightly different flow rates for each experiment. The results presented in Table3.2 where LCU refers to the liquid control unit, PT refers to pressure transmitters and temperature shortened as a temp. and Siemens

(MassFLO MASS 6000 combined with MASS 2100) mass flow meter referred to as flow meter.

Table 3.2: Experimental Results

	Unit	Module 1	Module 2	Module 3	Module 4
Module Material	-	Aluminum	Aluminum	Copper	Copper
Module Fin Density	-	25	85	25	85
Flow Rate from LCU	lpm	2	2.2	2.3	2.2
Flow Rate from Flow Meter	lpm	2.08	2.22	2.28	2.24
MassFlo Outlet Temp.	°C	26.43	26.43	26.37	26.42
Liquid Supply Temp. from LCU	°C	25	25	25.1	25
Liquid Return Temp. from LCU	°C	26	26	25.9	26
TC PA Side	°C	42.52	34.26	36.1	33.1
TC Driver	°C	30.71	28.96	28.87	28.19
TC PA Mid	°C	52.39	44.1	37.507	34.33
Pressure Drop from PT	bar	0.0582	0.8600	0.0454	0.9062
Pressure Drop from LCU	bar	0.3	1.1	0.3	1.2

3.3.1 Expected Measurement Uncertainty

The expected uncertainties of experimental measurement are determined according to manufacturer technical specifications of the corresponding equipment. The data sheets of the experimental equipment are presented in Appendix A. It should be noted that the accuracy information delivered by the manufacturer's needs account for the wide range of operating scenarios, therefore these accuracies are tended to be considerably higher than the actual measurement errors. The experimental measurement uncertainties are investigated statistically in the next section. The temperature measurements through J-Type thermocouples are collected by the Agilent 34970A data logger and the specification sheet of data logger clearly specifies the expected accuracy of temperature measurements according to the thermocouple type. Therefore the data logger accuracy of 1°C is determined as the actually expected accuracy of temperature readings instead of 2.2°C measurement accuracy stated in the thermocouple data sheet. The only mathematical operation conducted on experimental measurements is done during the calculation of the pressure drop. The pressure drop

calculated by the difference between the pressure transmitters located at the inlet and the outlet of the modules. Therefore the expected uncertainty of the pressure drop is determined as expected uncertainty of pressure transmitter multiplied by two in order to account for the worst case. The expected uncertainties of the experimental measurement are presented in Table 3.3.

Table 3.3: Expected uncertainties of the experimental measurements

Measurement	**Measurement Instrument**	**Expected Uncertainity**
Temperature	OMEGA J-Type Thermocouple	2.2 °C or 0.75% (higher)
Temperature	Agilent 34970A	1.0 °C
Flowrate	Siemens MassFLO 600	0.10%
Pressure	WIKA A-10 PT	0.30%
Pressure Drop	WIKA A-10 PT	0.60%

3.3.2 Repeatability Analysis

The repeatability analysis conducted on Module 4 experimental results since highest variations in measurements are observed in Module 4 experiments. Four sets of test data are captured for calculation of uncertainty of the measurements. The results of these experiments are presented in Table3.4.

Table 3.4: Experimental runs for repeatability analysis

Experiment Set	1	2	3	4
Flow Rate from Flow Meter (lpm)	2.24	2.23	2.23	2.24
MassFlo Temp, Outlet (°C)	26.42	26.59	26.67	26.52
Liquid Return Temp. from LCU (°C)	26	25.8	26.1	26.3
TC PA Side (°C)	33.1	32.6	34.89	35.2
TC Driver (°C)	28.19	27.7	27.95	28.52
TC PA Mid (°C)	34.33	34.09	34.15	34.58
Pressure Drop from PT (bar)	0.9062	0.9147	0.9089	0.8988

The readings from the liquid control unit (LCU) are kept out of this analysis since flow rate, pressure drop and temperature measurements from LCU stayed constant during these experimental runs. The LCU control software has a certain hysteresis and accuracy preset which unknown by the author. Therefore, these readings are not used in discussions. The calculation of measurement uncertainty is done according to the equation below.

$$U_j = \left| \frac{M_{i+1,jj} - M_{i,j}}{M_{i,j}} \right| x100 \tag{3.1}$$

Using the four sets of experimental data, average percentage repeatability accuracy is calculated by the following equation. Average percentage repeatability accuracy of experimental measurements of Module 4 is presented in Table3.5.

$$\overline{U} = \sum_{j=1}^{n} U_j/n \tag{3.2}$$

Table 3.5: Avarage percentage repeatability accuracy of experimental measurements

	Average Percentage Uncertainity (%)
Flow Rate from Flow Meter	0.22
MassFlo Temp, Outlet	0.38
Liquid Return Temp. from LCU	0.67
TC PA Side	2.36
TC Driver	1.17
TC PA Mid	0.53
Pressure Drop from PT	0.67

3.4 Discussion of Experimental Results

Experiments result in some inconsistencies with the numerical simulation results. The experimental results of alternative modules are compared with each other. Afterward the combination of simulation results and experimental results are discussed in order to determine the sources of mismatch between them.

In aluminum modules, the fin density increase from 25 FPI to 85 FPI resulted with 8.29 °C (15.8%) decrease in TC PA mid temperature and 0.8 bar (14.7 times) increase in pressure drop. In copper modules, the fin density increase from 25 FPI to 85 FPI resulted with 3.18 °C (8.5%) decrease in TC PA mid temperature and 0.86 bar (20 times) increase in pressure drop.

At 25 FPI fin density, the experimental results of copper module show that PA mid thermocouple temperatures are 14.9 °C (28.4%) lower than aluminum module while pressure drop is 0.013 bar lower in copper module compared to aluminum one.

At 85 FPI fin density, the experimental results of copper module show that PA mid thermocouple temperatures are 9.77 °C (22.2%) lower than an aluminum module. Moreover, the pressure drop is 0.047 bar higher in copper module compared to the aluminum one. This increase in pressure drop was unexpected therefore it required further attention. The pressure drop measurements of module 4 investigated in detail and experiments repeated several times as discussed in Section 3.3.2. A possible explanation for the unexpected experimental results is that the microchannel heat sink present in the module differs significantly from the original design due to manufacturing inaccuracies.

The comparison between the numerical simulation results and experimental results are presented in Table 3.6. Starting with the module 1 with aluminum and 25 FPI fin density, the temperatures of experimental results are within 3% margin with the numerical simulation results except for the driver thermocouple readings. It should be noted that the readings from the driver thermocouple (TC Driver) are not in first priority due to its relatively lower values. Whereas the pressure drop measurement is significantly lower than the simulation estimation by 34% difference. Module 1 is the only module in which the PA mid thermocouple reading is higher in experiment compared to the simulation results. This difference is believed to be caused by the maldistribution in flow rate among microchannels is much more severe than the prediction due to manufacturing inaccuracies in the first microchannel as seen in Figure 3.16. In module 2 experiments, temperature results are within 10% margin with the simulation estimations while pressure drop is 21% lower in experiments.

Table 3.6: Comparison of experimental results and numerical simulation results

		Simulation	Experiment
	Unit	**Module 1**	
TC PA mid	°C	50.91	52.39
TC PA side	°C	42.89	42.52
TC Driver	°C	28.58	30.71
DP	bar	0.088	0.058
	Unit	**Module 2**	
TC PA mid	°C	47.15	44.10
TC PA side	°C	38.38	34.26
TC Driver	°C	26.81	28.96
DP	bar	1.097	0.860
	Unit	**Module 3**	
TC PA mid	°C	41.81	37.51
TC PA side	°C	37.54	36.10
TC Driver	°C	28.44	28.87
DP	bar	0.041	0.045
	Unit	**Module 4**	
TC PA mid	°C	37.97	34.33
TC PA side	°C	33.00	33.10
TC Driver	°C	26.16	28.19
DP	bar	0.610	0.906

In module 3, experiments resulted with 4.3 °C decrease (10%) in mid-PA temperatures and 10.7% increase in pressure drop compared to numerical simulation results. Experimental results of module 3 are the best match with experiments while the inverse relationship between the temperatures and pressure drop is compatible with the theoretical knowledge.

In experimental results of module 4 are significantly different from the simulation results with about 50% increase in the pressure drop and 10% decrease in PA mid temperatures. With repeated experiment runs, the results stayed about the same. Therefore, it is determined that the experimental procedures are in order but there

must be some dimensional defects in microchannels affecting cooling performance and pressure drop significantly. The following section discusses these manufacturing inaccuracies in detail.

3.4.1 Manufacturing Inaccuracies in Microchannels

The mismatch between results of experiments and numerical simulations is determined to be caused by manufacturing inaccuracies in microchannel heat sinks. To support this claim, the alternative modules with microchannels are cut into three pieces with a water jet cutter and gathered pieces are investigated under a microscope. The photos of module pieces after water-jet cutting are presented in Figure 3.15

(a) (b)

Figure 3.15: Module pieces after water jet cutting (a) Module 1 (b) Module 2

The microscope images of module 1 are presented in Figure3.16. Several dimensional inaccuracies are found under the microscope as differences in channel width and height and small fin inclinations of up to 9 degrees. In addition, the fins are getting pointy towards the other opposing surface. Another defect in module 1 is that the first liquid channel has 0.662 mm width instead of 0.5 mm. Therefore, the liquid flow rate is higher in the first channel which resulted in a decrease in central liquid channels where liquid flow is needed the most.

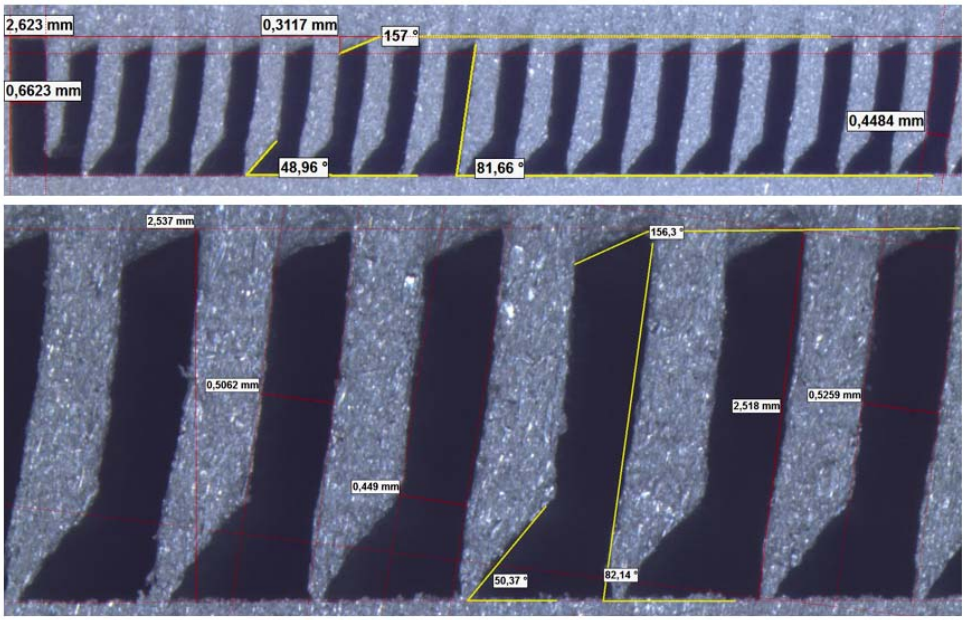

Figure 3.16: Microscope images of microchannel heat sink of module 1

The microscope images of module 2 are presented in Figure3.17. It is seen that the dimensional inaccuracies are more severe in the modules with higher fin densities. In module 2, some liquid channels are almost completely closed by inclinations towards each other while other channels have differences in width, height, and inclination. The liquid channel widths are in the range of 0.05 mm to 0.197 mm which suppose to be 0.15 mm. The fin inclinations are up to 14 degrees. The channel heights are in between 1.618 mm and 1.784 mm.

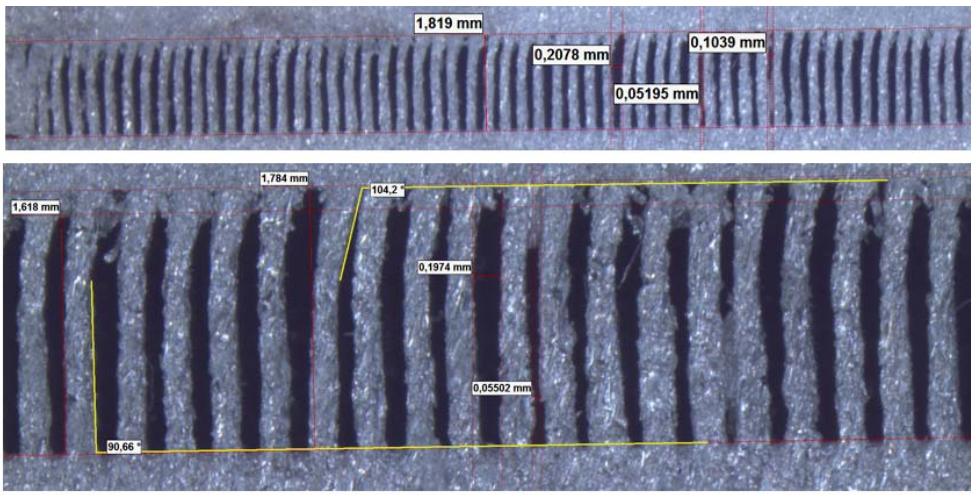

Figure 3.17: Microscope images of microchannel heat sink of module 2

The microscope images of module 3 are presented in Figure3.18. In module 3, some liquid channels have a serious burr at the root side. In addition, channels have differences in width, height, and inclination. The liquid channel widths are in the range of 0.37 mm to 0.51 mm which suppose to be 0.5 mm. The fin inclinations are up to 18 degrees. The channel heights are in between 4.36 mm and 5 mm.

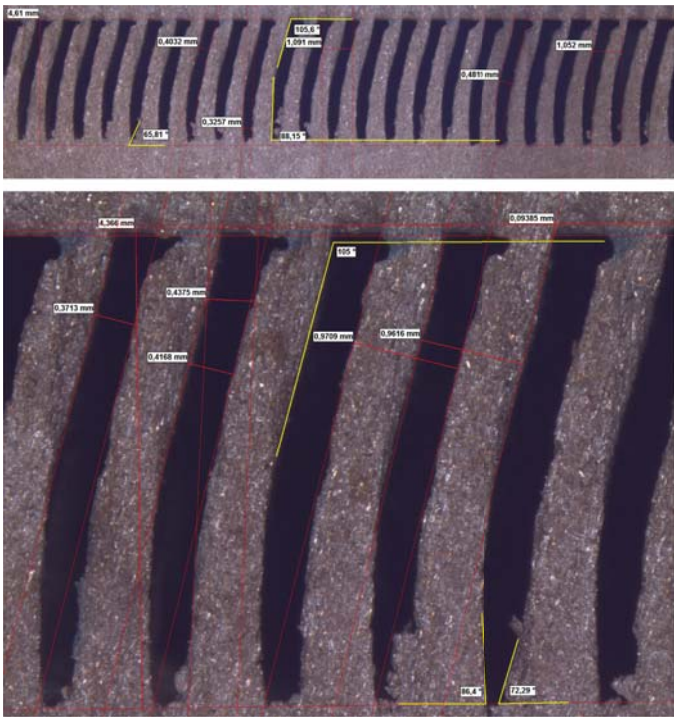

Figure 3.18: Microscope images of microchannel heat sink of module 3

The microscope images of module 4 are presented in Figure3.19. In module 4, the channels are filled with the subtracted particles of the water-jet cutting process due to softer characteristics of copper and smaller channel width of 0.15 mm. Even though the channels are not clear, their form remained the same. The same manufacturing inaccuracies are observed in module 4 as in other alternative modules. The liquid channel widths are in the range of 0.01 mm to 0.155 mm which suppose to be 0.15 mm. The fin inclinations are up to 16 degrees. The channel heights are in between 2.44 mm and 2.75 mm. The photos of the microchannel heat sink of module 4 prior to water jet cutting is presented in Figure3.20.

To summarize, several manufacturing inaccuracies are found in microchannel heat sinks of the modules. These manufacturing inaccuracies are further investigated in Chapter 4, where post-experiment numerical simulations are presented. The mi-

crochannel heat sinks of alternative modules are presented in Figure3.21.

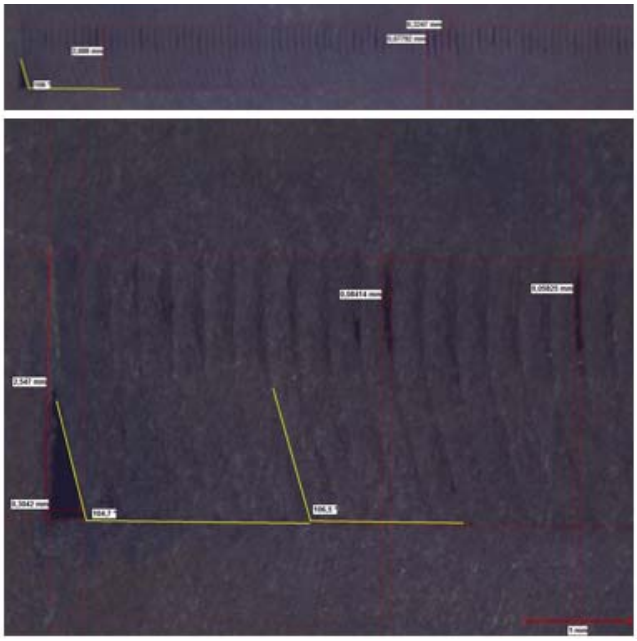

Figure 3.19: Microscope images of microchannel heat sink of module 4

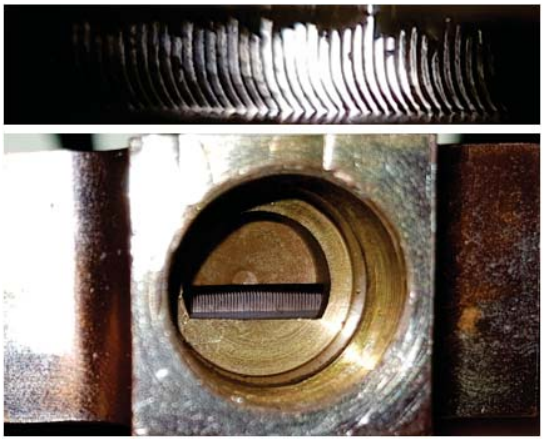

Figure 3.20: Photos of microchannel heat sink of module 4 prior to water jet cutting

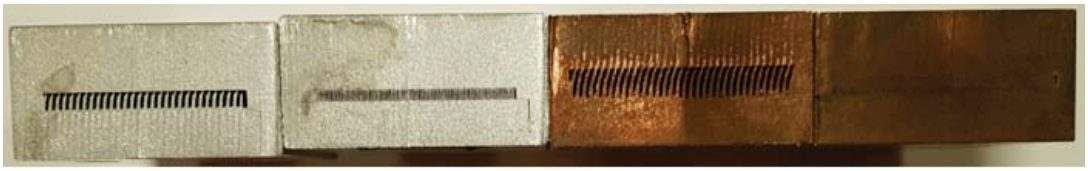

Figure 3.21: Photo of microchannel heat sinks of modules (left to right in numerical order)

CHAPTER 4

POST-EXPERIMENT INVESTIGATION OF MANUFACTURING ERRORS OF MICROCHANNELS ON HEAT SINK PERFORMANCE

As discussed in Chapter 3, the results of the experiments are not perfectly compatible with the numerical simulation results. In section 3.4.1 the microwave modules with microchannels from experiments are studied in detail in order to understand the possible sources of performance deviations. The module with the highest mismatch between results of simulation and experiment is found to be the Module 4 (copper module with 85 FPI fin density).

In this Chapter, the effect of manufacturing inaccuracies on the heat sink performance of microchannel heat sinks is numerically investigated. There are several dimensional errors observed in manufactured microchannels. The main manufacturing errors are determined to be the variations in channel width, fin height, and fin inclination. Although these errors are present together, they are investigated separately in order to understand their individual contributions to changes in performance. Afterward, the combination of these errors is analyzed and discussed.

4.1 Effect of Channel Width on Performance

For the post-experiment numerical simulations, module 4 is selected according to its significant mismatch between experimental results and numerical simulations. As discussed in detail in Section 3.4.1, the channel widths are in the range of 0.05 mm to

0.155 mm in module 4 where a channel with different widths is placed next to each other. After carefully investigating the microscope images, it is determined that the channels with different varying width are in a pattern which repeats itself at about every 4 channels. The fin widths are observed to have minimal variations, therefore, their dimensions are kept identical with 0.15 mm width. Three cases are determined to be numerically studied as shown in Table4.1.

Table 4.1: Simulation cases of channel width investigation

	Channel Width (mm)			
	Channel 1	Channel 2	Channel 3	Channel 4
Case 1	0.13	0.155	0.135	0.14
Case 2	0.12	0.155	0.115	0.135
Case 3	0.1	0.155	0.1	0.05

The numerical simulation runs are completed for three cases where flow equation is selected as enhanced two equation. The surface roughnesses are determined to be 25 microns. The results are presented in Table4.2.

Table 4.2: Numerical simulation results of channel width investigation

	Case 1	**Case 2**	**Case 3**
TC PA mid (°C)	37.92	37.88	37.34
TC PA side (°C)	32.93	32.89	32.71
TC Driver (°C)	26.13	26.11	26.1
DP (bar)	0.699	0.811	1.183

4.2 Effect of Channel Height on Performance

In Section 3.4.1, the channel height of module 4 is found to be in the range of 2.44 mm to 2.75 mm. Due to rather smaller variations in height compared to other types of inaccuracies, two cases are formed for investigations. The simulation cases and results are presented in Table4.3.

Table 4.3: Numerical simulation results of channel height investigation

	Case 1	**Case 2**
Channel Height (mm)	2.44	2.69
Max. Temperature (°C)	69	68.96
TC PA mid (°C)	38	37.98
TC PA side (°C)	33.05	33.02
TC Driver (°C)	26.2	26.17
Max. Flow Speed (m/s)	1.761	1.762
DP (bar)	0.6977	0.633

4.3 Effect of Channel Inclination on Performance

The liquid channel's angle of inclination is seen to be up to 16° from Section 3.4.1. The numerical analysis runs are performed according to two inclination cases with angle of an 8° and 16°, as shown in Table4.4.

Table 4.4: Numerical simulation results of channel height investigation

	Case 1	**Case 2**
Angle of Inclination	8°	16°
Max. Temperature (°C)	68.97	68.99
TC PA mid (°C)	38.025	38.03
TC PA side (°C)	33.1	33.1
TC Driver (°C)	26.18	26.184
Max. Flow Speed (m/s)	1.765	1.76544
DP (bar)	0.6714	0.7056

4.4 Investigation on Combination of Manufacturing Inaccuracies

In order to establish a close representation of module 4, the manufacturing inaccuracies are modeled together. For the combined defects analysis, case 2 from channel width investigations is determined to be the most accurate channel width combina-

tion according to the average channel width characteristics observed in microscope images. The channel height is determined to be 2.6 mm by taking an average of height variations. The results of numerical simulations with combined manufacturing defects are presented in Table4.5 where the angle of inclination is taken as 8° according to the module 4 average channel from.

Table 4.5: Numerical simulation results of combination of manufacturing inaccuracies compared to experimental results

	Simulation	**Experiment**	**Difference**	**Percentage Error**
TC PA mid (°C)	36.2	34.3	1.87	5.45%
TC PA side (°C)	32.6	33.1	-0.5	1.51%
TC Driver (°C)	26.0	28.2	-2.18	7.73%
DP (bar)	0.910	0.906	0.004	0.44%

4.5 Discussion of Post-Experiment Investigation of Manufacturing Inaccuracies of Microchannels

The experimental results of module 4 result in a more uniform temperature distribution compared to the numerical simulations. It is most probably caused by the air encapsulated within the insulation which acts as a conduction medium while introducing a limited natural convection. The results of pre-experiment and post-experiment numerical simulations are presented in Table 4.7 along with the experimental results. The results showed that the post-experiment numerical simulation of the combined manufacturing errors provides a much closer representation of the actual case with better temperature and pressure estimations. Especially for the pressure drop estimations, the post-experiment numerical model proves the necessity of careful modeling of microchannel dimensions and manufacturing inaccuracies in order to achieve a successful numerical estimations with the below 1% accuracy. It is also seen that the effect of manufacturing inaccuracies on temperature distribution can be ignorable for less temperature sensitive applications in comparison to RF PA chips considering the maximum temperature difference of 1.8 °C between numerical simulations.

The pressure drop increase caused by the manufacturing inaccuracies can be vital for microchannel heat sinks with softer materials. In literature, researches can be found where the implementation of microchannels within the chip substrates such as silicon are studied to achieve a shorter heat flow path between the heat source and the coolant. For such cases, long-term reliability issues introduced by increased pressure drop should be considered. Moreover, the post-experimental simulation results support that the modeling of manufacturing errors by taking the average of varying channel dimensions is a satisfactory approach.

Table 4.6: Results of pre-experiment and post-experiment numerical simulations compared to experimental results for module 4

	Numerical Simulations Results		**Experimental Results**
	Pre-Experiment	**Post-Experiment**	
TC PA mid (°C)	37.97	36.2	34.3
TC PA side (°C)	33	32.6	33.1
TC Driver (°C)	26.16	26	28.2
DP (bar)	0.61	0.91	0.906

CHAPTER 5

CONCLUSIONS

Electronic components with extreme heat fluxes can operate under steady-state conditions by the implementation of a thermal management design using single-phase liquid cooling with microchannels. In the present study, the thermal management design of a microwave module with heat dissipating PA chips is presented.

As discussed in Chapter 3, the results of the experiments are not perfectly compatible with the numerical simulation results. In Section 3.4.1 the microwave modules with microchannels from experiments are studied in detail in order to understand the possible sources of performance deviations. The microscope images showed that the dimensions of microchannels differ from the original design due to variations of height, width and inclination angle. The module with the highest mismatch between results of simulation and experiment is found to be the module 4 (copper module with 85 FPI fin density). In Chapter 4, the manufacturing inaccuracies are modeled for post-experiment numerical simulations where effects of individual defects are studied.

Especially for designs where low weight is not a priority, the material selection of copper should be considered rather than aluminum. The material selection with higher thermal conductivity provides significant performance improvement without creating a demand for more pumping power.

Although the increase in fin density of microchannel heat sinks resulted in cooling performance improvement, the pressure drop along the module increase dramatically by up to 20 times. Therefore, a thermal designer should consider microchannel heat sink with 85 FPI fin density or above only if the design requirements cannot be sat-

isfied by any other method and the costs of manufacturing and pumping power are secondary objectives.

From the results of this study, it is deduced that the manufacturing inaccuracies in microchannels affect heat sink performance especially pressure drops. According to the manufacturing techniques, different types of defects can be found in microchannel dimensions which result in pressure drop increase of up to two times.

In the future studies, further investigations on manufacturing defects of microchannel should be conducted by using a wider range of cold plates which are manufactured by different techniques. Moreover, the scope of experimental studies can be expanded by considering additional material alternatives for microchannels and different coolant liquid types. In addition, a future study may be conducted for varying liquid flow rates and liquid inlet temperature.

REFERENCES

[1] G. E. Moore, "Cramming more components onto integrated circuits, reprinted from electronics, volume 38, number 8, april 19, 1965, pp. 114 ff.," *IEEE Solid-State Circuits Society Newsletter*, vol. 11, no. 3, pp. 33–35, 2006.

[2] G. E. Moore *et al.*, "Progress in digital integrated electronics," in *Electron Devices Meeting*, vol. 21, pp. 11–13, 1975.

[3] S. Mehendale, A. Jacobi, and R. Shah, "Fluid flow and heat transfer at micro- and meso-scales with application to heat exchanger design," *Applied Mechanics Reviews*, vol. 53, no. 7, pp. 175–193, 2000.

[4] S. G. Kandlikar, M. Steinke, S. Tian, and L. A. Campbell, "High-speed photographic observation of flow boiling of water in parallel mini-channels," in *35th Proceedings of National Heat Transfer Conference*, Citeseer, 2001.

[5] S. G. Kandlikar, "Fundamental issues related to flow boiling in minichannels and microchannels," *Proc. Experimental Heat Transfer, Fluid Mechanics and Thermodynamics, Thessaloniki*, pp. 129–146, 2001.

[6] S. G. Kandlikar and W. J. Grande, "Evolution of microchannel flow passages: thermohydraulic performance and fabrication technology," in *ASME 2002 International Mechanical Engineering Congress and Exposition*, pp. 59–72, American Society of Mechanical Engineers, 2002.

[7] M. Richter, P. Woias, and D. Weiβ, "Microchannels for applications in liquid dosing and flow-rate measurement," *Sensors and Actuators A: Physical*, vol. 62, no. 1-3, pp. 480–483, 1997.

[8] I. Mudawar, "Assessment of high-heat-flux thermal management schemes," *IEEE Transactions on Components and Packaging Technologies*, vol. 24, no. 2, pp. 122–141, 2001.

[9] B. K. Singh, G. S. Yadav, and A. Yadav, "Study on electric discharge machining and scope for new era," 2016.

[10] Wire EDM Fundamentals. Retrieved October 1, 2018, from http://www.reliableedm.com/Complete

[11] How accurate is wire EDM. Retrieved October 1, 2018, from https://www.micropulsewest.com/our-blog/how-accurate-is-wire-edm/.

[12] C. Öztoprak and İ. Tarı, “Micro-channel cold plate dimensional precision effects on performance,” in *2nd Thermal and Fluid Engineering Conference (TFEC)*, pp. 105–110, American Society of Thermal and Fluids Engineers (ASTFE), 2017.

[13] A Brief Explanation of CNC Machines and How They Work. Retrieved October 1, 2018, from https://wiki.mcneel.com/rhino/cncbasics.

[14] T. Duda and L. V. Raghavan, “3d metal printing technology,” *IFAC-PapersOnLine*, vol. 49, no. 29, pp. 103–110, 2016.

[15] R. Kukowski, “Mdt: Micro deformation technology,” in *ASME 2003 International Mechanical Engineering Congress and Exposition*, pp. 305–308, American Society of Mechanical Engineers, 2003.

[16] Micro Deformation Technology. Retrieved August 28, 2018, from https://www.microcooling.com/technology/micro-deformation-technology/.

[17] C. Fuentes, “Microwave power amplifier fundamentals,” *A Giga Tronics Technical white power*, pp. 1–24, 2008.

[18] R. S. Pengelly, S. M. Wood, J. W. Milligan, S. T. Sheppard, and W. L. Pribble, “A review of gan on sic high electron-mobility power transistors and mmics,” *IEEE Transactions on Microwave Theory and Techniques*, vol. 60, no. 6, pp. 1764–1783, 2012.

[19] C. Öztoprak and E. Erkek, “Thermal performance improvement of an air-cooled gan-based solid state power amplifier,” in *Thermal Investigations of ICs and Systems (THERMINIC)*, pp. 1–6, IEEE, 2017.

[20] Qorvo, "50 Watt Discrete Power GaN on SiC HEMT," TGF2023-2-10 datasheet, Jan. 2017 (Revision D).

[21] D. Murdock and M. Woods, “Gan thermal analysis for high-performance systems,” *White Paper*, 2014.

[22] A. Venkatachalam, W. James, and S. Graham, “Electro-thermo-mechanical modeling of gan-based hfets and moshfets,” *Semiconductor Science and Technology*, vol. 26, no. 8, p. 085027, 2011.

[23] S. Rajasingam, J. Pomeroy, M. Kuball, M. Uren, T. Martin, D. Herbert, K. Hilton, and R. Balmer, “Micro-raman temperature measurements for electric field assessment in active algan-gan hfets,” *IEEE Electron Device Letters*, vol. 25, no. 7, pp. 456–458, 2004.

[24] M. Azarifar, *An Analytical Method for The Accurate and Effective Thermal Modelling of AlGaN/GaN HEMTS*. PhD thesis, Middle East Technical University, 2017.

[25] G. Riedel, J. Pomeroy, K. Hilton, J. Maclean, D. Wallis, M. Uren, T. Martin, and M. Kuball, “Nanosecond timescale thermal dynamics of algan/gan electronic devices,” *IEEE Electron Device Letters*, vol. 29, no. 5, pp. 416–418, 2008.

[26] A. İ. Işık, *X-BAND High Power Gan Power Amplifier Design and Implementation*. PhD thesis, Middle East Technical University, 2016.

[27] EMC Technology, "CVD Diamond Chip 20 Watts," CR0402D datasheet, Nov. 2016 (Form 423F123 Revision A).

[28] EMC Technology, "CVD Diamond Chip 50 Watts," CT0505D datasheet, Nov. 2016 (Form 423F125 Revision A).

[29] Stäubli, "CGO/CGD Thermal Management and Cooling of Electronics," CGO/CGD datasheet, Apr. 2017 (Form RD7050300C).

[30] Software Library. ANSYS, Workbench version 19.0, Retrieved August 1, 2018.

[31] V. C. P. H. C. Chen, “Near-wall turbulence models for complex flows including separation,” *AIAA Journal*, vol. 26, no. 6, pp. 641–648, 1988.

[32] T. Jongen, “Simulation and modeling of turbulent incompressible flows,” *PhD thesis, EPF Lausanne, Lausanne, Switzerland*, 1992.

[33] P. Spalart and S. Allmaras, “A one-equation turbulence model for aerodynamic flows. technical report aiaa-92-0439,” *American Institute of Aeronautics and Astronautics*, 1992.

APPENDIX A

TECHNICAL SPECIFICATIONS OF THE COMPONENTS AND EQUIPMENT USED IN EXPERIMENTAL SETUP

A.1 Technical Specifications of OMEGA J-Type Thermocouple

Revised Thermocouple Reference Tables

TYPE J

Reference Tables
N.I.S.T.
Monograph 175
Revised to
ITS-90

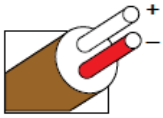

Thermocouple Grade

Iron vs. Copper-Nickel

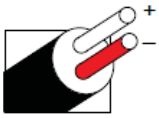

Extension Grade

MAXIMUM TEMPERATURE RANGE

Thermocouple Grade
32 to 1382°F
0 to 750°C

Extension Grade
32 to 392°F
0 to 200°C

LIMITS OF ERROR
(whichever is greater)
Standard: 2.2°C or 0.75%
Special: 1.1°C or 0.4%

COMMENTS, BARE WIRE ENVIRONMENT:
Reducing, Vacuum, Inert; Limited Use in Oxidizing at High Temperatures;
Not Recommended for Low Temperatures

TEMPERATURE IN DEGREES °C
REFERENCE JUNCTION AT 0°C

Thermoelectric Voltage in Millivolts

°C	-10	-9	-8	-7	-6	-5	-4	-3	-2	-1	0	°C
0	0.000	0.050	0.101	0.151	0.202	0.253	0.303	0.354	0.405	0.456	0.507	0
10	0.507	0.558	0.609	0.660	0.711	0.762	0.814	0.865	0.916	0.968	1.019	10
20	1.019	1.071	1.122	1.174	1.226	1.277	1.329	1.381	1.433	1.485	1.537	20
30	1.537	1.589	1.641	1.693	1.745	1.797	1.849	1.902	1.954	2.006	2.059	30
40	2.059	2.111	2.164	2.216	2.269	2.322	2.374	2.427	2.480	2.532	2.585	40
50	2.585	2.638	2.691	2.744	2.797	2.850	2.903	2.956	3.009	3.062	3.116	50
60	3.116	3.169	3.222	3.275	3.329	3.382	3.436	3.489	3.543	3.596	3.650	60
70	3.650	3.703	3.757	3.810	3.864	3.918	3.971	4.025	4.079	4.133	4.187	70
80	4.187	4.240	4.294	4.348	4.402	4.456	4.510	4.564	4.618	4.672	4.726	80
90	4.726	4.781	4.835	4.889	4.943	4.997	5.052	5.106	5.160	5.215	5.269	90

A.2 Technical Specifications of Agilent 34970A Data Logger

Agilent 34970A
Data Acquisition/Switch Unit

Operating Characteristics[4]

Single Channel Measurement Rates [5]

Function	Resolution [9]	reading/s
dcV, 2-wire Resistance	6½ digits (10 plc)	6 (5)
	5½ digits (1 plc)	57 (47)
	4½ digits (0.02 plc)	490
Thermocouple	0.1°C (1 plc)	49 (47)
	(0.02 plc)	280
RTD, Thermistor	0.01°C (10 plc)	6 (5)
	0.1°C (1 plc)	47 (47)
	1°C (0.02 plc)	280
acV	6½ Slow (3 Hz)	0.14
	6½ Med (20 Hz)	1
	6½ Fast (200 Hz)	8
	6½ [6]	100
Frequency, Period	6½ digits (1s gate)	1
	5½ digits (100 ms)	9
	4½ digits (10 ms)	70

Related Literature	Pub. number
Accessories for the 34970A Data Acquisition/Switch Unit, data sheet	5966-4443EN

System Specifications

Scanning Inputs	
Analog	34901A, 34902A, and 34908A multiplexer channels
Digital	34907A digital in and totalize
Scan list	Scans channels in ascending order
Scan Triggering	
Source	Interval, external, button press, software, or on monitor channel alarm
Scan count	1 to 50,000 or continuous
Scan interval	0 to 99 hours; 1ms step size
Channel delay	0 to 60 seconds per channel; 1 ms step size
External trig delay	<300 µs. With monitor on <200 ms
External trig jitter	<2 ms
Alarms	
Analog inputs	Hi, Lo, or Hi + Lo evaluated each scan
Digital inputs	34907A digital in maskable pattern match or state change 34907A totalize: Hi limit only
Monitor channel	Alarm evaluated each reading
Alarm Outputs	4 TTL compatible Selectable TTL logic Hi or Lo on fail
Latency	5 ms (typical)
Memory	
	Battery backed, 4 year typical life[1]
Readings	50,000 with timestamp Readable during scan
States	5 instrument states with user label
Alarm Queue	Up to 20 events with channel number, reading, and timestamp
System Features	
Per-channel Math	Individual Mx + B scaling and Min/Max/Average calculated real time
Power Fail Recovery	Resumes scanning automatically
Relay maintenance	Counts each relay closure and stores on module User resettable
Real-time clock	Battery-backed, 4-year typical life[1]
General Specifications	
Power Supply	100V/120V/220V/240V ±10%
Power Line Frequency	45 Hz to 66 Hz automatically sensed
Power Consumption	12 W (25 VA peak)
Operating Environment	Full accuracy for 0°C to 55°C Full accuracy to 80% R.H. at 40°C
Storage Environment	-40°C to 70°C[1]
Weight	Net: 3.6 kg (8.0 lbs)
Safety	Conforms to CSA, UL-1244, IEC 1010 Cat I
RFI and ESD	CISPR 11, IEC 801/2/3/4

Accuracy Specifications ±(% of reading + % of range)[1]

	Range[3]	Frequency, etc.	24 Hour[2] 23°C±1°C	90 Day 23°C±5°C	1 Year 23°C±5°C
DC Voltage					
	100.0000 mV		0.0030 + 0.0035	0.0040 + 0.0040	0.0050 + 0.0040
	1.000000 V		0.0020 + 0.0006	0.0030 + 0.0007	0.0040 + 0.0007
	10.00000 V		**0.0015 + 0.0004**	**0.0020 + 0.0005**	**0.0035 + 0.0005**

Temperature	Type	1-Year Accuracy[9]		Extended Range 1-Year Accuracy[9]	
Thermocouple[10]	B	1100°C to 1820°C	1.2°C	400°C to 1100°C	1.8°C
	E	-150°C to 1000°C	1.0°C	-200°C to -150°C	1.5°C
	J	**-150°C to 1200°C**	**1.0°C**	**-210°C to -150°C**	**1.2°C**
	K	-100°C to 1200°C	1.0°C	-200°C to -100°C	1.5°C
	N	-100°C to 1300°C	1.0°C	-200°C to -100°C	1.5°C

A.3 Technical Specifications of WIKA Type A-10 Pressure Transmitter

Pressure transmitter
For general industrial applications
Model A-10

WIKA data sheet PE 81.60 · 10/2017

Special features

- Measuring ranges from 0 ... 20in WC to 0 ... 15,000 psi (0 ... 0.05 to 0 ... 1,000 bar)
- Non-linearity 0.25 % or 0.5 %
- Output 4 ... 20 mA, DC 0 ... 10 V, DC 0 ... 5 V and others
- Electrical connection: Angular connector form A and C, circular connector M12 x 1, cable outlet 6 ft
- Process connection G ¼ A DIN 3852-E, ¼ NPT and others

Accuracy specifications

	Standard
Non-linearity per BFSL (IEC 61298-2)	
■ Measuring range ≤ 0.1 bar	≤ ±0.5 % of span
■ Measuring range > 0.1 bar	≤ ±0.5 % of span
Measuring deviation of the zero signal [2) 3)]	
■ 4 ... 20 mA	≤ ±0.3 % of span
■ DC 0 ... 10 V	≤ ±0.5 % of span
■ DC 0 ... 5 V [4)]	≤ ±0.6 % of span
■ DC 1 ... 5 V	≤ ±0.3 % of span
■ DC 0.5 ... 4.5 V	≤ ±0.3 % of span
■ DC 0.5 ... 4.5 V ratiometric	≤ ±0.3 % of span
Accuracy at room temperature [5)]	
■ Measuring range ≥ 0.6 bar	≤ ±1 % of span
■ Measuring range ≥ 0.4 bar	≤ ±1.2 % of span
■ Measuring range ≥ 0.25 bar	≤ ±1.3 % of span
■ Measuring range ≥ 0.16 bar	≤ ±1.5 % of span
■ Measuring range ≥ 0.1 bar	≤ ±1.8 % of span
■ Measuring range ≥ 0.05 bar	≤ ±2.4 % of span

with standard cable outlet, unshielded

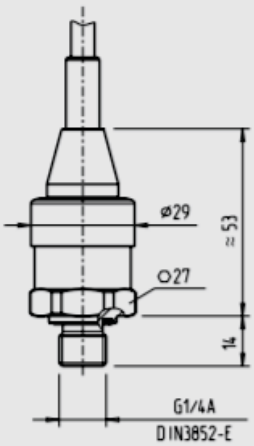

Weight: approx. 80 g

Non-repeatability (per IEC 61298-2)
Measuring range ≤ 0.1 bar: ≤ 0.2 % of span
Measuring range > 0.1 bar: ≤ 0.1 % of span

Signal noise
≤ ±0.3 % of span
(≤ ±0.2 % of span on request)

Temperature error at 0 ... 80 °C (32 ... 176 °F)
Typical: ≤ ±1 % of span
Maximum: ≤ ±2.5 % of span
Maximum ≤ ±1.5 % of span on request

Long-term drift (per IEC 61298-2)
Measuring ranges ≤ 0.1 bar: ≤ ±0.5 % of span [1)]
Measuring ranges ≤ 0.4 bar: ≤ ±0.2 % of span
Measuring ranges > 0.4 bar: ≤ ±0.1 % of span

A.4 Technical Specifications of EMC Technology CR0402D CVD Diamond Resistor Chip 20 Watts

RESISTOR
CVD DIAMOND CHIP 20 WATTS

EMC Technology

DATA SHEET **PART SERIES: CR0402D** SHEET 1 OF 2 Dwg 1011115 EN 13-3904 Revision -

FEATURES

- Small Size - Light Weight
- Highest Thermal Performance Possible
- Excellent Peak Power Capability
- Rugged Passivated TaN Film
- Moisture Resistant
- Pure Gold Input Pads
- Wire Bondable or Solderable
- High Power

APPLICATIONS

- Broadcast
- Higher Power Filters
- High Power Amplifiers
- Instrumentation
- Isolators
- Military
- Satellite Communications
- Phased Array Radar

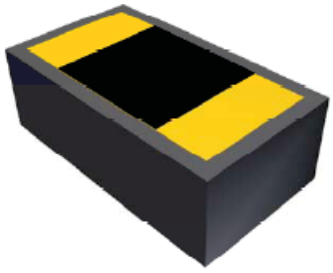

ORDERING INFORMATION

Part Identifier:

CR0402D X, 5

Resistance

SPECIFICATIONS

1.0 ELECTRICAL

Resistance:	50 Ω & 100 Ω, ± 5%
Frequency Range:	DC – 30 GHz
Capacitance:	0.09 pF Typical
Input Power CW:	20 Watts
Peak Power:	200 Watts (1 µs pulse width/1% duty cycle)

2.0 ENVIRONMENTAL

Operating Temperature:	-55°C to +150°C
Storage Temperature:	-55°C to +150°C

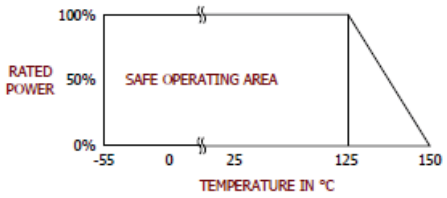

3.0 MARKING

Unit Marking:	None

4.0 QUALITY ASSURANCE

Sample Inspect Per MIL-STD-105, Level II, 1.0% AQL.

- Visual and Mechanical Inspection for Conformance to Outline Drawing
- Measure DC Resistance
- Data Retention - Standard

5.0 PACKAGING

Standard:	Waffle Packaging
Optional:	Tape and Reel

Form 423F124 Rev A Cage Codes: 24602 / 2Y194 www.emc-rflabs.com • +1 772-286-9300

Specifications are Subject to Change Without Notice *AS 9100, ISO 9001 and 14001 Certified*

A.5 Technical Specifications of EMC Technology CT0505D CVD Diamond Resistor Chip 50 Watts

TERMINATION
CVD DIAMOND CHIP 50 WATTS

EMC Technology

DATA SHEET **PART SERIES: CT0505D** SHEET 1 OF 2 Dwg 1010525 EN 13-3904 Revision -

FEATURES

- Small Size - Light Weight
- Highest Thermal Performance Possible
- Excellent Peak Power Capability
- Rugged Passivated TaN Film
- Moisture Resistant
- Pure Gold Input Pads
- Wire Bondable or Solderable
- High Power

APPLICATIONS

- Broadcast
- Higher Power Filters
- High Power Amplifiers
- Instrumentation
- Isolators
- Military
- Satellite Communications
- Phased Array Radar

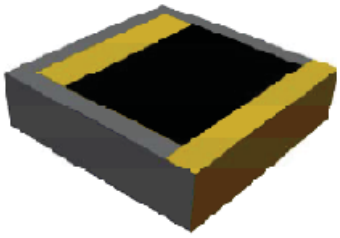

ORDERING INFORMATION

Part Identifier: CT0505D

SPECIFICATIONS

1.0 ELECTRICAL

Nominal Impedance:	50 Ω ± 5%
Frequency Range:	DC – 20 GHz
Input Power CW:	50 Watts
Peak Power:	500 Watts (1 µs pulse width/1% duty cycle)
VSWR:	1.6:1 Max

2.0 ENVIRONMENTAL

Operating Temperature:	-55 °C To +150 °C
Storage Temperature:	-55 °C To +150 °C
Temperature Coefficient:	±200 PPM/°C Max

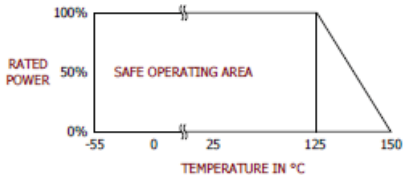

3.0 MARKING

Unit Marking:	None

4.0 QUALITY ASSURANCE

Sample Inspect Per ANSI/ASQC Z1.4 General Inspection, Level II, 1.0% AQL.

- Visual and Mechanical Inspection for Conformance to Outline Drawing
- Measure DC Resistance
- Data Retention - Standard

5.0 PACKAGING

Standard:	Waffle Packaging

Form 423F125 Rev A **Cage Codes: 24602 / 2Y194** *Specifications are Subject to Change Without Notice* **www.emc-rflabs.com • +1 772-286-9300** *AS 9100, ISO 9001 and 14001 Certified*

A.6 Technical Specifications of Siemens MASSFLO 6000 Coriolis Flowmeter

	MASS 6000 Compact IP 67 and 19" IP 20 version
Measurement of	Mass flow [kg/s], volume flow [l/s], fraction [%], Brix, density [kg/m^3], temperature [°C]
Current output	
Current	0-20 mA or 4-20 mA
Load	< 800 ohm
Time constant	0-30 s adjustable
Digital output	
Frequency	0-10 kHz, 50% duty cycle
Time constant	0-30 s adjustable
Active	24 V d.c., 30 mA, 1 KΩ ≤ R_{load} ≤ 10 KΩ, short-circuit-protected
Passive	3-30 V d.c., max. 110 mA, 1 KΩ ≤ R_{load} ≤ 10 KΩ
Relay	
Type	Change-over relay
Load	42 V / 2 A peak
Functions	Error level, error number, limit, direction
Digital input	11-30 V d.c.
Functionality	Start/hold/continue batch, zero-point adjust, reset totalizer 1/2, force output, freeze output
Galvanic isolation	All inputs and outputs are galvanically isolated, isolation voltage 500 volts
Cut-off	
Low-flow	0-9.9% of maximum flow
Limit function	Mass flow, volume flow, fraction, density, sensor temperature
Totalizer	Two eight-digit counters for forward, net or reverse flow
Display	Background illumination with alphanumerical text, 3 × 20 characters to indicate flow rate, totalized values, settings and faults.
	Reverse flow indicated by negative sign
Zero-point adjustment	Manual via keypad or remote via digital input
Ambient temperature	Operation: –20 to +50°C
	During storage: –40 to +70°C (Humidity max. 95%)
Communication	Prepared for client mounted add-on modules
Enclosure compact IP 67	
Material	Fibre glass-reinforced polyamide
Rating	IP 67 to IEC 529 and DIN 40050 (1 m w.g. for 30 min.)
Mechanical load	18-1000 Hz random, 3.17G rms, in all directions, to IEC 68-2-36
Enclosure 19"	
Material	Aluminium/steel (DIN 41494)
Rating	IP 20 to IEC 529 and DIN 40050 (1 m w.g. for 30 min.)
Mecanical load	18-1000 Hz random, 3.17G rms, in all directions, to IEC 68-2-36
Supply voltage	115/230 V a.c. +10% to –10%, 50-60 Hz
	18-30 V d.c. or 20-30 V a.c.
Power consumption	230 V a.c.: 9 VA max.
	24 V d.c.: 6 W I_N = 250 mA, I_{ST} = 2A (30 msec)
EMC performance	
Emission	EN 50081-1 (Light industry)
Immunity	EN 50082-2 (Industry)
Ex-approval	[EEx ia] II C, DEMKO Ex99E.125729X
Maintenance	The flowmeter has a built-in error log/pending menu which should be inspected on a regular basis
Fuse	T 400 mA, T 250 V (IEC 127). Not replaceable by operator